

國立交通大學

電子工程學系

電子研究所碩士班

碩士論文

二維完美匹配層應用於多重解析法
之光學微影模擬

Two-Dimensional Perfectly Matched
Layer Applied to Multiresolution
Time-Domain Method for Optical
lithography simulation

研究生：曾建彰

指導教授：羅正忠博士

中華民國九十六年七月

二維完美匹配層應用於多重解析法
之光學微影模擬

Two-Dimensional Perfectly Matched
Layer Applied to Multiresolution
Time-Domain Method for Optical
lithography simulation

研究生：曾建彰

Student：Jian-Zhang Zeng

指導教授：羅正忠博士

Advistor：Dr. Jen-Chung Lou



A Thesis
Submitted to Institute of Electronics
College of Electrical and Computer Engineering
National Chiao Tung University
in Partial Fulfillment of the Requirements
for the Degree of Master of Science
in Electronic Engineering
July 2007
Hsinchu, Taiwan, Republic of China

中華民國九十六年七月

二維完美匹配層應用於多重解析法 之光學微影模擬

研究生:曾建彰

指導教授:羅正忠

國立交通大學

電子工程學系

電子研究所碩士班



隨著光微影技術向極限推進時，極化效應正變得更加明顯[20]。由於橫向電波和橫向磁波之間結合的不同造成在圖罩(photomask)表面的散射及在晶圓的極化使得成像品質降低[16]。因此我們需要以馬克斯威爾方程式快速且精確的計算晶圓裡的成像。

著眼此點，我們企圖將完美匹配層(PML)應用在多重解析法。於是我們先找出一對 Battle-Lemarie 系的尺度和小波函數。在文獻中[1][2]，使用這個可以當作完整基底函數的集合被稱為多重解析度分析。因此我們表明，將多重解析法應用於離散馬克斯威爾方程式的新計畫稱為 MRTD。在此篇論文中，為了簡化我們將只使用尺度函數來開發模擬程式(S-MRTD)。除此之外我們將使用此程式搭配完美吸收邊界層(PML)來模擬開放的二維相移圖罩結構的繞射電磁分析。

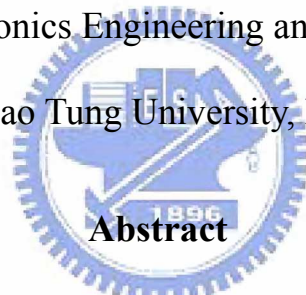
Two-Dimensional Perfectly Matched Layer Applied to Multiresolution Time-Domain Method(MRTD) for optical lithography simulation

Student: Jian-Zhang Zeng

Advisor: Dr. Jen-Chung Lou

Department of Electronics Engineering and Institute of Electronics

National Chiao Tung University, Hsinchu, Taiwan



Polarization effects are becoming more pronounced [20] as optical lithography technique is pushed towards its limit. Photomask topography scattering, and wafer polarization effects caused by differences in coupling between transverse electric and transverse magnetic waves degrade image quality.[16] Therefore we need to fast and rigorous calculation Latent images in wafer by Maxwell's equations.

To solve this problem,we attempt to apply" Perectly Matched Layer" (PML) to "Multiresolution Time-Domain Method". Thus we find a pair of cubic spline Battle-Lemarie scaling and wavelet functions. In literature[1][2],the use of these functions as a complete set of basis functions is called multiresolution analysis. Thus we show that the application of multiresolution analysis in the method of moments for the discretization of Maxwell's equations leads to new multiresolution time-domain

(MRTD) schemes. In this paper, for simplicity, we will use the scaling function scheme(S-MRTD) only to develop simulation program. In addition, this program is applied to the rigorous simulation of diffraction from two-dimension open phase-shifting mask structure. Open boundaries are simulated by the use of a novel formulation of the perfect matching layer(PML) absorber.



誌謝

兩年的碩士學業很快就要劃下句號了，首先我想感謝我的指導教授羅正忠博士，由於您的細心指導與教誨，讓我在研究上與許多做人處事上都有莫大的收穫，真的使我受益匪淺，在這裡對老師致上我內心最高的謝意，感謝您兩年來的教導。

此外，我還要感謝張仲興與胡國信學長的指導以及您所留下來的寶貴資源讓我在研究上得以順利解決許多難題及模擬實驗，謹此致上最誠摯的謝意。同時也要感謝曾經一起同甘苦的同學們：人傑、忠樂、彥銘、德安、智仁、睿龍、宏仁、俐婷、大峰、信智、勝凱，謝謝你們在生活及精神上給予的支持。也要感謝跟我住在一起的室友們：士銘、小誠、飛龍師、小P，謝謝你們豐富我的生活。另外也要感謝彤彤姑娘的支持與鼓勵讓我有勇氣克服萬難。

最後我要感謝父母苦心的栽培與一再的鼓勵，以及你們無怨無悔的付出讓我無後顧之憂完成我的碩士學業。在此獻上我內心最深的感恩，辛苦你們了：爸、媽、以及姐姐。

Contents

Abstract (Chinese)	i
Abstract (English)	ii
Acknowledgements	iv
Contents	v
Figure Captions	vii
Chapter 1 Introduction	
1.1 Introduction to Optical Lithography.....	1
1.2 Motivation.....	3
1.2.1 Overview of Optical Imaging System Modeling.....	3
1.2.2 Rigorous Electromagnetic Simulation.....	4
1.2.3 Absorbing Boundary Conditions.....	5
1.2.4 Numerical Solution of Maxwell's Equations by MRTD.....	5
1.3 Organization of This Thesis.....	5
Chapter 2 Boundary Conditions for the Finite-Difference Time-Domain(FDTD) Method	
2.1 The FDTD method and the Yee equations.....	11
2.2 A Perfectly Matched Layer for the absorption of Electromagnetic Waves.....	14
2.2.1-The theory and derivation of the PML medium.....	14
(a) Definition of the PML medium.....	14
(b) Propagation of a plane wave in a PML medium.....	15
(c) Transmission of a Wave through PML-PML Interfaces.....	18
2.3 Numerical Stability Condition.....	23
2.4 Numerical Dispersion Relation.....	23

Chapter 3 Using Battle-Lemarie Scaling Function Based
Multiresolution time-domain(MRTD) schemes

3.1 Fundamentals Of Multiresolution Analysis.....29
3.2 Derivation of the S-MRTD Scheme.....30
3.3 Numerical Stability condition.....35
3.4 Numerical Dispersion.....36

Chapter 4 Simulation and Conclusion

4.1 S-MRTD formulation.....42
4.2 Simulation results.....44
4.3 Conclusion.....45

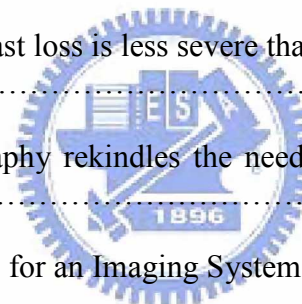
References.....52



Figure Captions

Chapter 1

Figure.1-1 Integrated circuit fabrication process.....	7
Figure.1-2 Frequently-encountered circuit geometries.....	7
Figure.1-3 (a) Optical diffraction blurs dark-bright transitions in the layout. (b) Photoresist nonlinearity can turn the rather sloppy image into vertical profiles.....	7
Figure.1-4 Schematic of an exposure system.....	8
Figure.1-5 High-NA vs low-NA.....	8
Figure.1-6 Aerial images of a 1:1 line-space pattern with a period of $0.7\lambda/NA$. The NA is 0.965.....	9
Figure.1-7 Latent image contrast loss is less severe than aerial image degradation.....	9
Figure.1-8 Immersion lithography rekindles the need to examine wafer polarization effects.....	10
Figure.1-9 A simplified Model for an Imaging System.....	10



Chapter 2

Figure.2-1 Maxwell's equations are solved over a cubic grid using the FDTD method. The field components are staggered over the grid	25
Figure.2-2 (a)The electric field $E_z(i,j,k)$ is calculated by summing up the magnetic field values of the four neighboring nodes. The magnetic field components are assumed to be constant along the line segments 1-2,2-3,3-4,and4-1,and the electric field E_z is assumed to be constant over the square surface bounded by 1-2-3-4	
(b) The magnetic field $H_z(i+1/2,j+1/2,k+1/2)$ is calculated by summing up the electric field values of the four neighboring nodes. The electric field components are assumed to be constant along the line segments 1-2,2-3,3-4,and4-1,and the magnetic field H_z is assumed to be constant over the square surface bounded by 1-2-3-4.	
.....	25

Figure.2-3 The transverse electric problem.....	26
Figure.2-4 Interface lying between two PML media.....	26
Figure.2-5 The PML technique.....	27
Figure.2-6 Upper-right part of the FDTD grid.....	27
Figure.2-7 graphs results obtained using this procedure that illustrate the variation of the numerical phase velocity with propagation angle in a two-dimensional FDTD grid.....	28

Chapter 3

Figure.3-1 Cubic spline Battle-Lemarie scaling function in space domain.....	38
Figure.3-2 Cubic spline Battle-Lemarie scaling function in spectral domain.....	38
Figure.3-3 Cubic spline Battle-Lemarie wavelet function in space domain.....	39
Figure.3-4 Cubic spline Battle-Lemarie wavelet function in spectral domain....	39
Table I Coefficients $a(i)$	40
Figure.3-5 Phase error of MRTD employing scaling functions only: Graphs the variation of the numerical phase error in degrees per wavelength as a function of the parameter, $1/s(1/C)$, for the case $n_a = 12$	41

Chapter 4

Figure.4-1 The PML regions are labeled as shown in the diagram.....	46
Figure.4-2 MRTD simulation result.....	46
Figure.4-3 MRTD simulation result.....	47
Figure.4-4 MRTD simulation result.....	47
Figure.4-5 MRTD simulation result.....	48
Figure.4-6 MRTD simulation result.....	48

Figure.4-7 A new contact hole 2D-PSM design.....49

Figure.4-8 E-D curve of 100nm contact-hole by the 2D-PSM design.....49

Figure.4-9 A new contact hole 3D-PSM design.....50

Figure.4-10 E-D curve of 100nm contact-hole by the 3D-PSM design.....50

Table 1: FDTD(left) versus MRTD(right) for 2D Quartz object.....51

Figure.4-11 Dispersion characteristics of FDTD and S-MRTD, $Q= c\Delta t / \Delta x$ 51



Chapter 1

Introduction

1.1 Introduction to Optical Lithography

In the manufacture process,[3] the different layout layers are delineated sequentially onto the silicon wafer by photolithography[4]. This module is the predominant enabler for the 40% per year increase in transistor count per chip. Illustrated in Figure.1-1, the photolithography process starts by coating the silicon substrate with a layer of photoresist. Transistors or wiring patterns are then imaged onto the photoresist by optical lithography. After development of the resist latent image, materials are removed from or deposited onto the wafer by processing steps such as etching, deposition, chemical mechanical polishing (CMP), and ion implantation. The photoresist is subsequently removed, leaving the substrate ready for another cycle of processing steps. Fabrication is complete after cycling a silicon wafer through these processing modules 30 to 40 times.

Circuit geometries printed by optical lithography can be generalized into the two classes illustrated in Figure.1-2(a): line-space and contacts. As a simplification, lines and spaces are usually assumed periodic with period p and dimension d [Figure.1-2(b)]. For example, image of a periodic line-space array with a 1 : 1 duty ratio is shown in Figure.1-3(a). Ideally transition from dark to bright regions should be sharp so that the photoresist is either exposed or unexposed. But optical diffraction blurs the transition. Fortunately photoresist development nonlinearity can turn the rather sloppy images into vertical profiles, as illustrated in Figure.1-3(b).

The photolithography imaging system is shown schematically in Figure.1-4. A narrowband light source of wavelength λ is placed at the focal plane of the condenser represented by lens L1, illuminating the photomask by Koehler's method[5]. Image of the photomask, template that contains the layout geometries, is formed by the projection optics onto the wafer. The projection optics is represented by the two lenses L2 and L3 in the Figure1-4; in actual systems it can consist of more than 30 lenses[6]. Because of the Fourier transforming property of lens L2[7], energy transmitted through the photomask forms a distribution in the pupil plane that is proportional to the mask spectrum. Low-spatial-frequency components pass closer to the center of the pupil whereas higher frequency components are nearer the peripheral of the pupil. The highest frequencies are cut off by the pupil. Observing from the wafer plane, the image-forming rays are restricted in angular extent by the pupil, subtending an angle θ at the wafer. The sine of the angle θ is the numerical aperture (NA) of the system: $NA = \sin \theta$. In the pupil plane an image of the source is formed. For a circular source and pupil in conventional optical lithography, the partial coherence factor σ is defined as the ratio between the sizes of the source image (the effective source) and the pupil. For the system drawn in Figure1-4.

$$\sigma = \frac{a}{b}.$$

Mathematically the imaging process can be described by[5]

$$I(x, y) = \int_{-\infty}^{+\infty} \dots \int \tilde{J}(f, g) \tilde{P}(f + f', g + g') \tilde{P}^*(f + f'', g + g'') \cdot \tilde{O}(f', g') \tilde{O}^*(f'', g'') e^{+i2\pi[(f' - f'')x + (g' - g'')y]} df' dg' df'' dg'' dfg,$$

where $I(x, y)$ is the image intensity at location (x,y) on the wafer, \tilde{J} is the effective source, \tilde{P} is the pupil function, \tilde{O} is the mask spectrum, and the asterisk * denotes complex conjugation.

Similar to Rayleigh's resolution criterion, resolution of an exposure system scales with (λ/NA) . It is customary to represent the critical dimension (CD) of the printed feature size as

$$CD = k_1 \cdot \frac{\lambda}{NA},$$

where k_1 is a process-related factor measuring the ease of lithography. Smaller dimensions can be printed by decreasing the wavelength, increasing the numerical aperture, and reducing k_1 . All three measures must be applied to sustain Moore's law and to achieve the ultimate resolution.

1.2 Motivation

1.2.1 Overview of Optical Imaging System Modeling

A modern, complex optical imaging system can have several lens, polarizer, mask, aperture, wafer, and pupil components and is usually very large in relation to the wavelength of light. Thus it is not practical to simulate the imaging system with the FDTD method. However, the science of optics can be applied to the imaging system components for modeling purposes. The Hopkins theory of partially coherent imaging is commonly used to calculate aerial images in lithography.

To print or inspect smaller features, optics designers build optics with higher numerical apertures (Figure.1-5). For numerical apertures exceeding 0.5 to 0.6, the paraxial approximations made in scalar imaging theory are invalid and theory has been extended by Daniel C. Cole et al. [8] who removed the paraxial ray approximation in the projection optic model. This led to the "Radiometric Correction Factor" that extended the usefulness of the projection optic model to numerical apertures in the

range 0.6 to 0.7. But even with the radiometric correction factor, the scalar theory is deficient for high numerical aperture lithography (NA) due to the differences in the way TE and TM plane waves behave, especially at the image plane where highly oblique plane waves exist. M S.Yeung[9] realized that a vector formulation is required for high NA imaging inside thin film stacks and generalized the Hopkins' formula for vector fields. But he then points out that, upon entering the photoresist, the plane waves bend towards the normal reducing their degree of obliquity, and reverts back to a scalar theory which he claims is "sufficient" for the practical simulation of aerial images in planar thin-film structures for numerical apertures at least as high as 0.6. But the recent interest in immersion lithography rekindles the need to examine wafer polarization effects. With the incident medium being a liquid

of refractive index n_{liquid} higher than 1, resolution of immersion lithography is

$$CD = k_1 \cdot \frac{\lambda}{n_{liquid} NA}$$

For 193-nm lithography, a promising immersion liquid is water having a refractive index of 1.43, giving a 43% resolution improvement. With the use of an immersion liquid, ray angles in resist becomes larger, resulting in more severe polarization effects.(see Figure.1-6,7,8 we can know)

1.2.2 Rigorous Electromagnetic Simulation

As device dimensions are pushed deeper and deeper into the submicron regime ,polarization and other complex electromagnetic effects that arise because of mask topography are becoming increasingly more important to model.

(Figure.1-9) The science of Fourier Optics is applied to model the source, illumination optic and projection optic. Rigorous ElectroMagnetic

Simulation (REMS) may be required to model the object (photomask).

The formation of the aerial image inside a film stack(Latent image) at the image plane may be model either by REMS or by thin-film-stack theory.[11]

1.2.3 Absorbing Boundary Conditions

In 1994, Berenger published a paper[10] on a new type of boundary condition which he named “Perfectly Matched Layers” or PML. The boundary condition is essentially a non-physical material with the special property that it absorbs electromagnetic radiation without reflection for all frequencies and angles of incidence. In this paper, the new boundary condition was implemented into S-MRTD and is explained in Chapter 2.

1.2.4 Numerical Solution of Maxwell's Equations by MRTD

In this paper, the recently developed multiresolution time-domain (MRTD) method[12] is applied to fast and rigorous mask diffraction simulation, to overcome the limitations of FDTD. An outline of the MRTD formulation is described in Chapter 3. In addition, In chapter 4, using a 2D scattering example to allow the use of an extremely fine computational mesh to achieve good convergence.

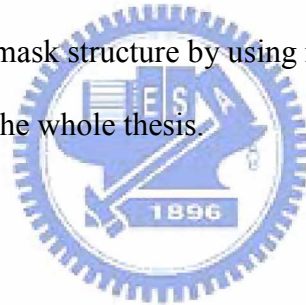
1.3 Organization of This Thesis

The thesis includes four chapter. In chapter 1, we make an introduction to describe the background and polarization effects of the optical lithography and the role in the semiconductor industry that optical lithography is playing. In addition, we make a

brief to describe simple concept of the imaging process mathematically. Then, we describe the motivation of this thesis. Finally, we introduce PML and MRTD techniques respectively.

In chapter2, we will first specify a numerical scheme for solving the Maxwell's equations, used by Yee.[13] Yee was one of the first to replace Maxwell's equations by a set of finite difference equations. Then, we will illustrate PML technique for two-dimensional problems.

In chapter3, we first explain the most important properties of the multiresolution analysis. Then, we will only derive the S-MRTD scheme for a homogeneous medium. Finally, in chapter4, we will use S-MRTD and PML schemes to rigorously simulate two-dimensional phase-shifting mask structure by using matlab. Then, we will make a conclusion with simulation in the whole thesis.



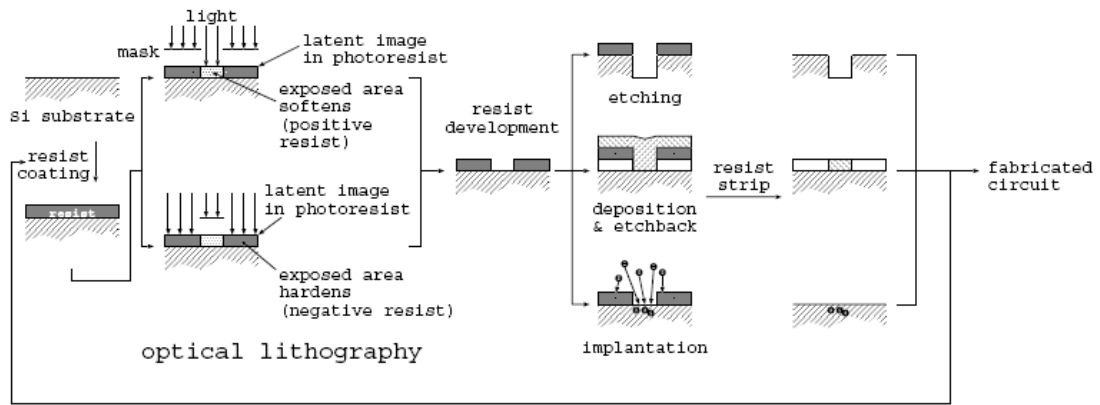


Figure.1-1 Integrated circuit fabrication process

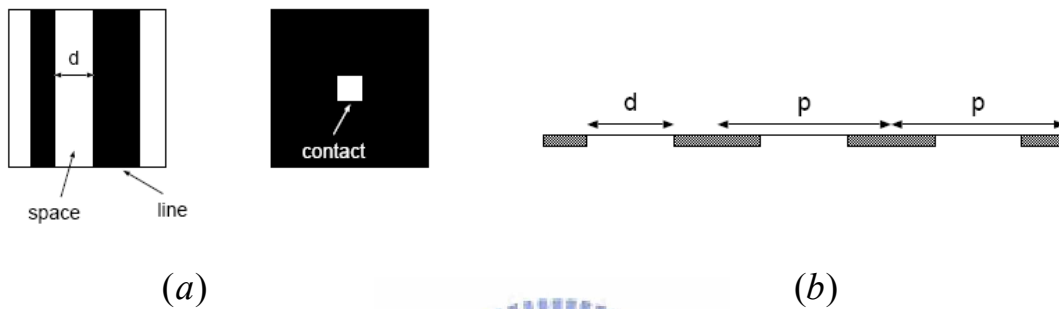


Figure.1-2 Frequently-encountered circuit geometries.
 (a) lines, spaces, and contacts (b) periodic line-space pattern

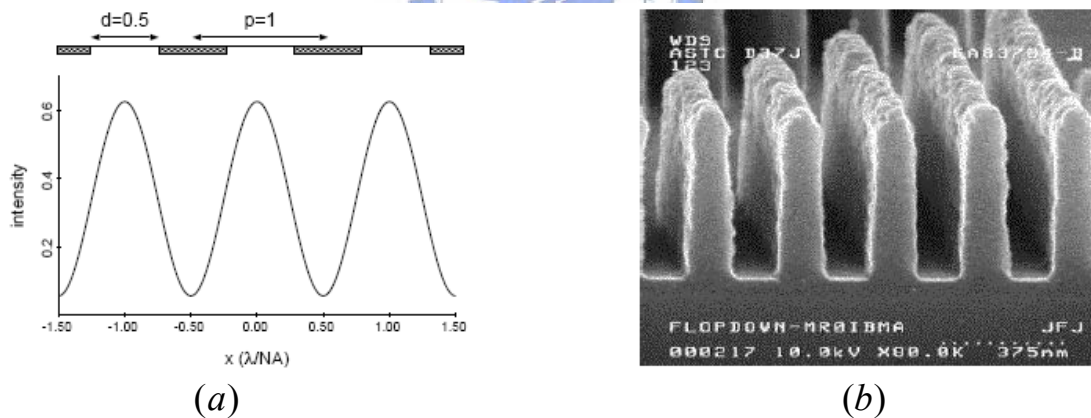


Figure.1-3 (a) Optical diffraction blurs dark-bright transitions in the layout. (b) Photoresist nonlinearity can turn the rather sloppy image into vertical profiles.

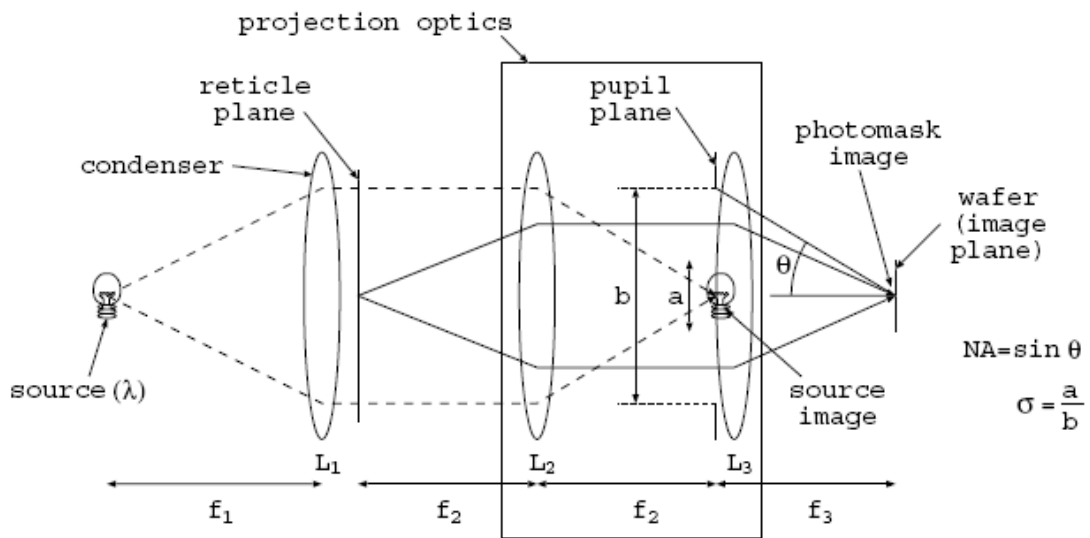


Figure.1-4 Schematic of an exposure system.

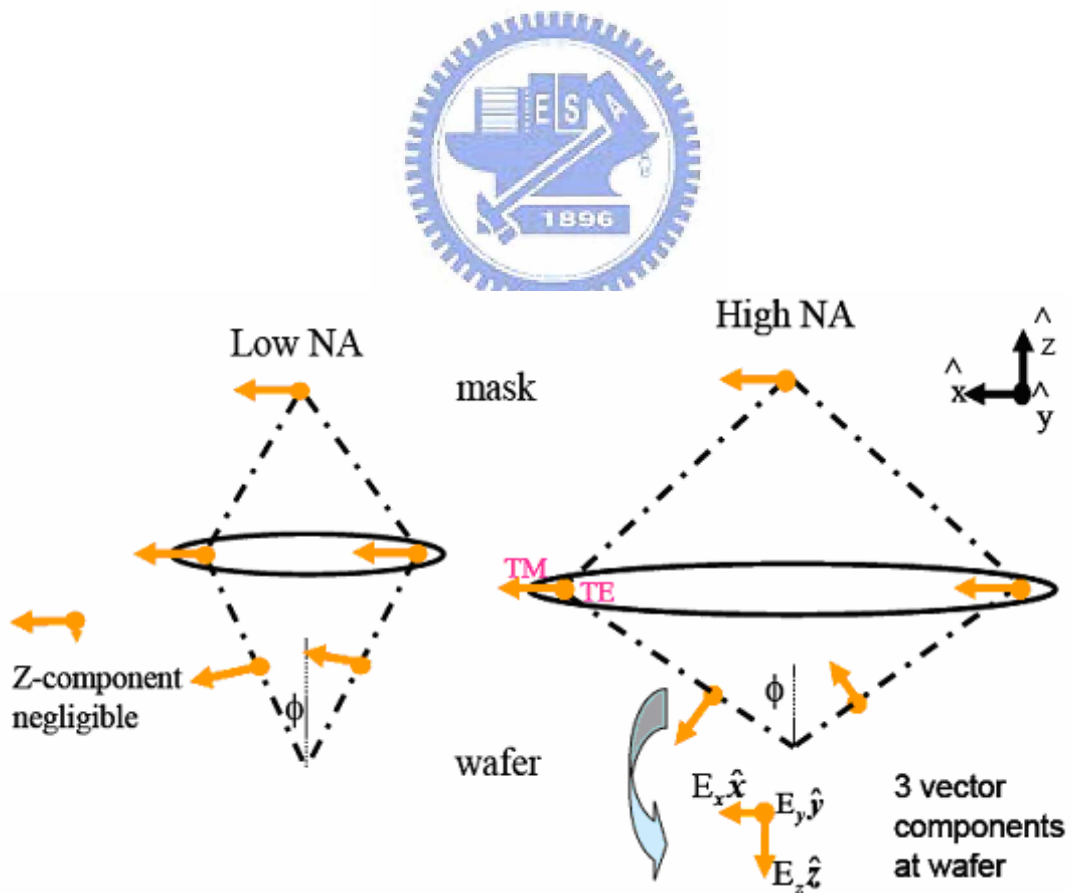


Figure.1-5 High-NA vs low-NA

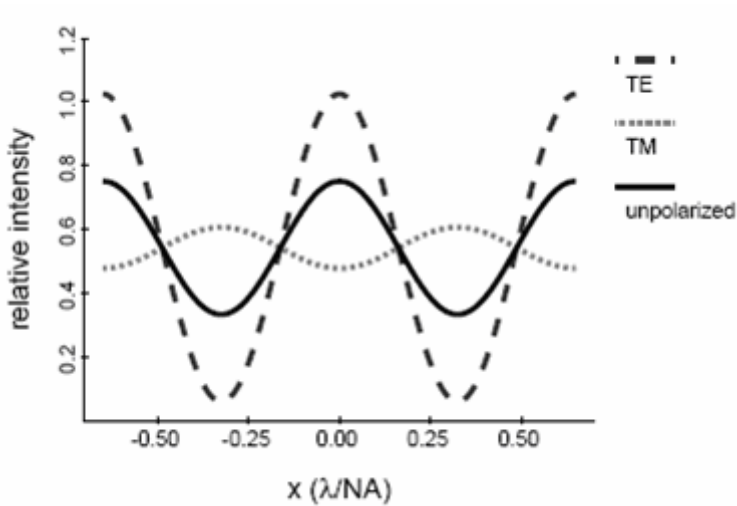


Figure.1-6 Aerial images of a 1:1 line-space pattern with a period of $0.7\lambda/NA$. The NA is 0.965.

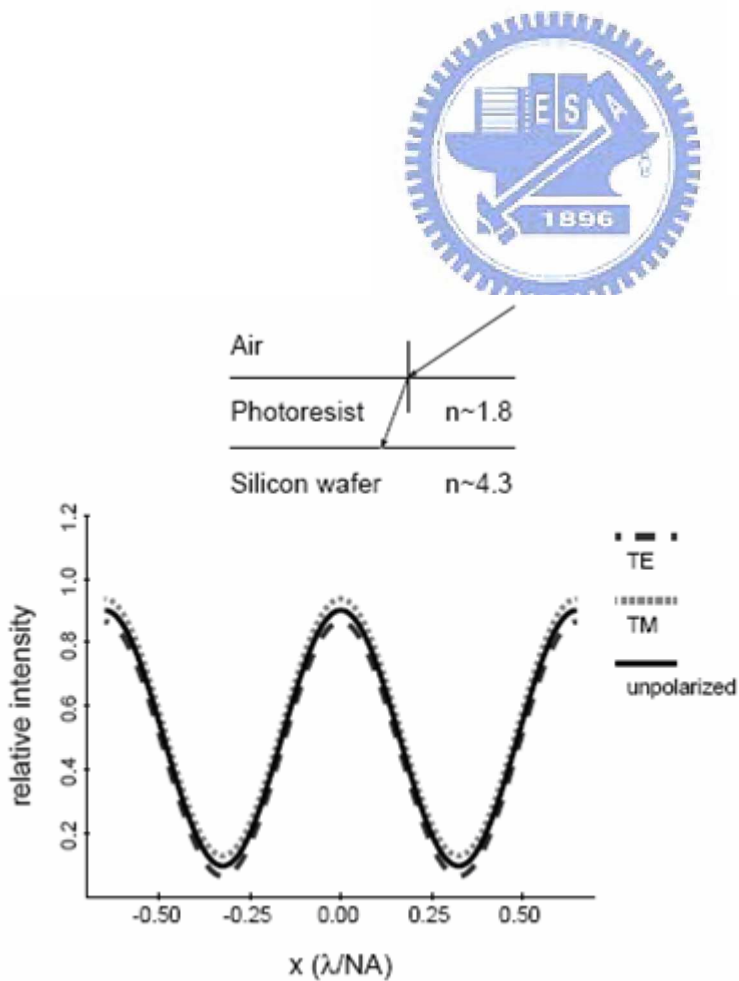


Figure.1-7 Latent image contrast loss is less severe than aerial image degradation.

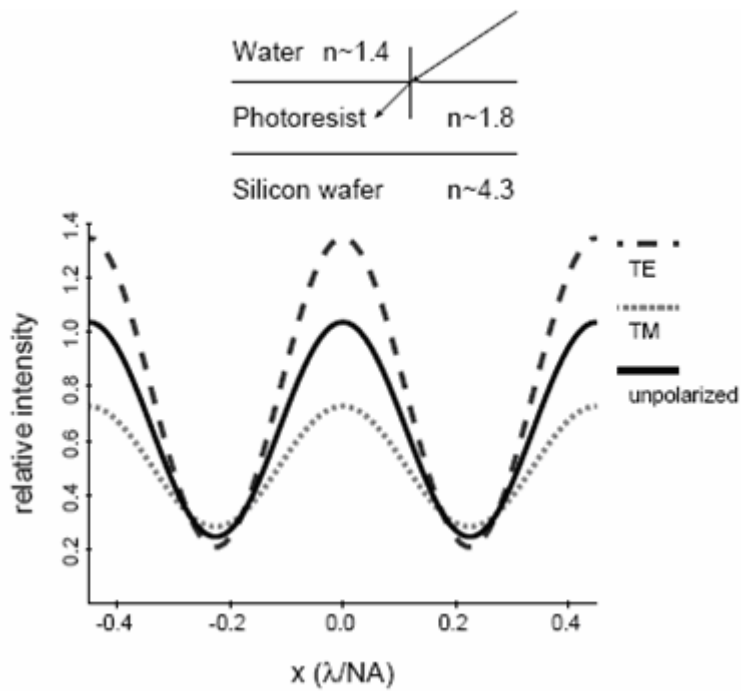


Figure.1-8 Immersion lithography rekindles the need to examine wafer polarization effects.

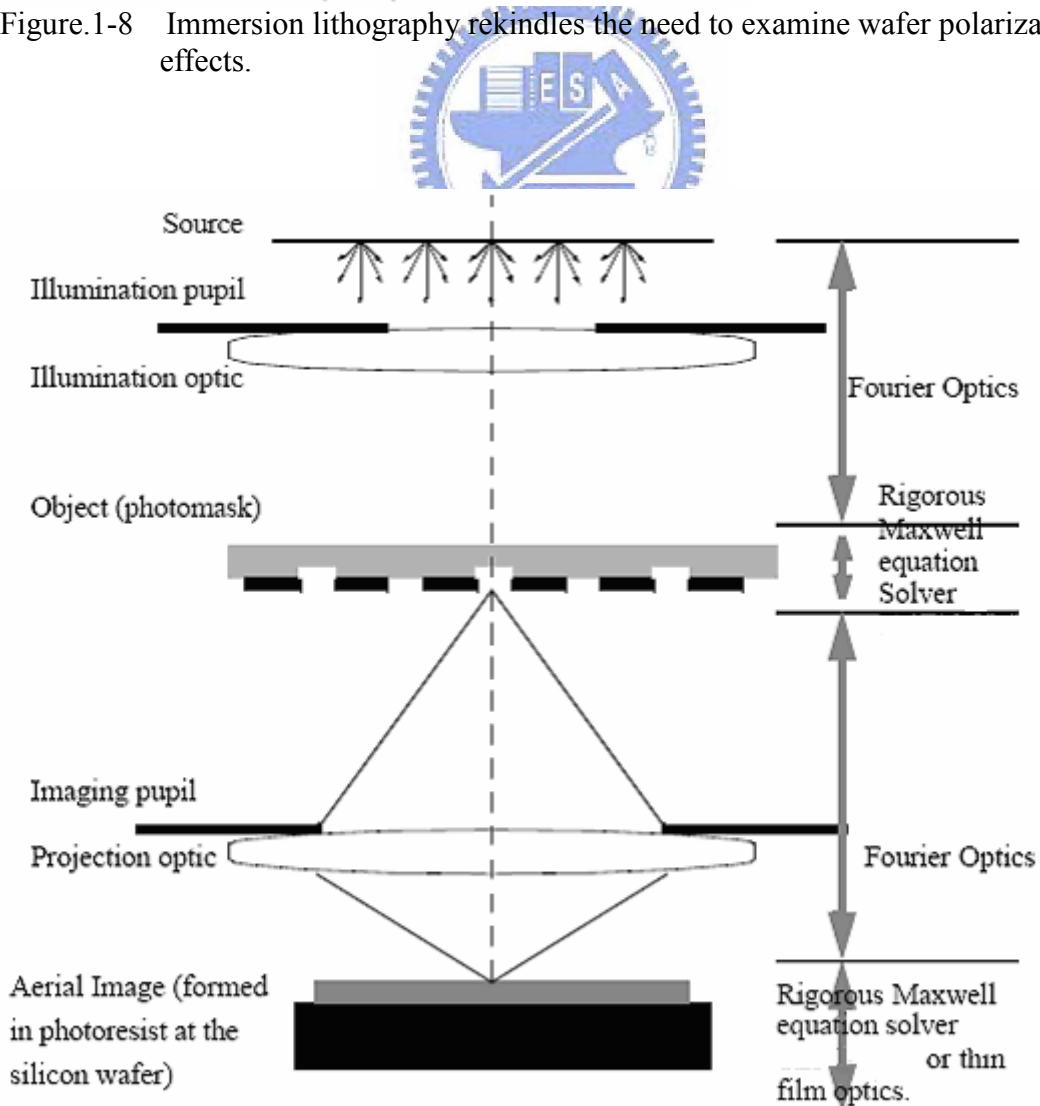


Figure.1-9 A simplified Model for an Imaging System

Chapter 2

Boundary Conditions for the Finite-Difference Time-Domain(FDTD) Method

2.1 The FDTD method and the Yee equations

The continuous form of the Maxwell equations for linear, isotropic, non-magnetic, nondispersive materials are written:

$$\nabla \times \vec{H} = \frac{\partial \vec{D}}{\partial t} + \vec{J} \quad (1.a)$$

$$\nabla \times \vec{E} = -\frac{\partial \vec{B}}{\partial t} \quad (1.b)$$

with the constitutive relations:

$$\begin{aligned} \vec{D} &= \epsilon \vec{E} \\ \vec{B} &= \mu \vec{H} \\ \vec{J} &= \sigma \vec{E} \end{aligned} \quad (2)$$



Where ϵ , μ , and σ are, respectively, the permittivity, permeability, and conductivity of the material. In general, the parameters ϵ , μ , and σ are functions of the frequency of the electromagnetic wave. For the application in hand, however,

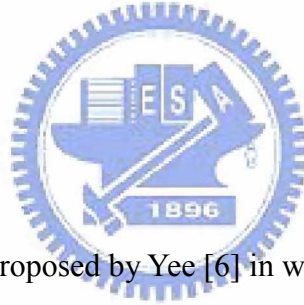
they are assumed to be constant because of monochromatic excitation. Using Stokes' theorem, (1.ab) and (2) can be re-written in the weak form

$$\oint_l \vec{H} \cdot d\vec{l} = \int_s \left\{ \frac{\partial \vec{D}}{\partial t} + \vec{J} \right\} \cdot d\vec{S} \quad (3)$$

$$\oint_l \vec{E} \cdot d\vec{l} = -\int_s \frac{\partial \vec{B}}{\partial t} \cdot d\vec{S} \quad (4)$$

Where $\oint_l \vec{F} \cdot d\vec{l}$ and $\int_s \vec{F} \cdot d\vec{S}$ represent, respectively, the line integral and surface integral of a variable \vec{F} . (1.ab) and (2) also are equivalent to the following system of scalar equations:

$$\begin{aligned}
 -\frac{\partial B_x}{\partial t} &= \frac{\partial E_z}{\partial y} - \frac{\partial E_y}{\partial z}, \\
 -\frac{\partial B_y}{\partial t} &= \frac{\partial E_x}{\partial z} - \frac{\partial E_z}{\partial x}, \\
 \frac{\partial B_z}{\partial t} &= \frac{\partial E_x}{\partial y} - \frac{\partial E_y}{\partial x}, \\
 \frac{\partial D_x}{\partial t} &= \frac{\partial H_z}{\partial y} - \frac{\partial H_y}{\partial z} - J_x, \\
 \frac{\partial D_y}{\partial t} &= \frac{\partial H_x}{\partial z} - \frac{\partial H_z}{\partial x} - J_y, \\
 \frac{\partial D_z}{\partial t} &= \frac{\partial H_y}{\partial x} - \frac{\partial H_x}{\partial y} - J_z.
 \end{aligned} \tag{5}$$



Following the FDTD method proposed by Yee [6] in which the differential δt is replaced by Δt and by Δx , (3)(4) or (5) are solved using a cubic grid in which the field components are staggered and occupy distinct locations in space as shown in Fig. 2.1 The surface integral and line integral are thus evaluated on square surfaces as shown in Fig. 2.2. This discretization scheme[17] leads to three scalar equations in two-dimensional analysis for the transverse electric (TE) or the transverse magnetic (TM) polarization, but six equations in three-dimensional analysis for the field components E_x, E_y, E_z, H_x, H_y , and H_z :

$$\begin{aligned}
E_x^{n+1}(i, j, k) &= \alpha E_x^n(i, j, k) + \beta [H_x^{n+(1/2)}(i, j - \frac{1}{2}, k) \\
&\quad - H_x^{n+(1/2)}(i, j + \frac{1}{2}, k) \\
&\quad + H_y^{n+(1/2)}(i + \frac{1}{2}, j, k) \\
&\quad - H_y^{n+(1/2)}(i - \frac{1}{2}, j, k)] \\
E_y^{n+1}(i, j + \frac{1}{2}, k + \frac{1}{2}) &= \alpha E_y^n(i, j + \frac{1}{2}, k + \frac{1}{2}) \\
&\quad + \beta [H_z^{n+(1/2)}(i - \frac{1}{2}, j + \frac{1}{2}, k + \frac{1}{2}) \\
&\quad - H_z^{n+(1/2)}(i + \frac{1}{2}, j + \frac{1}{2}, k + \frac{1}{2}) \\
&\quad + H_x^{n+(1/2)}(i, j + \frac{1}{2}, k + 1) \\
&\quad - H_x^{n+(1/2)}(i, j + \frac{1}{2}, k)]
\end{aligned}$$

$$\begin{aligned}
E_x^{n+1}(i + \frac{1}{2}, j, k + \frac{1}{2}) &= \alpha E_x^n(i + \frac{1}{2}, j, k + \frac{1}{2}) \\
&\quad + \beta [H_y^{n+(1/2)}(i + \frac{1}{2}, j, k) \\
&\quad - H_y^{n+(1/2)}(i + \frac{1}{2}, j, k + 1) \\
&\quad + H_z^{n+(1/2)}(i + \frac{1}{2}, j + \frac{1}{2}, k + \frac{1}{2}) \\
&\quad - H_z^{n+(1/2)}(i + \frac{1}{2}, j - \frac{1}{2}, k + \frac{1}{2})] \\
H_x^{n+(1/2)}(i + \frac{1}{2}, j + \frac{1}{2}, k + \frac{1}{2}) &= H_x^{n-(1/2)}(i + \frac{1}{2}, j + \frac{1}{2}, k + \frac{1}{2}) \\
&\quad - \gamma [E_x^n(i + \frac{1}{2}, j, k + \frac{1}{2}) \\
&\quad - E_x^n(i + \frac{1}{2}, j + 1, k + \frac{1}{2}) \\
&\quad + E_y^n(i + 1, j + \frac{1}{2}, k + \frac{1}{2}) \\
&\quad - E_y^n(i, j + \frac{1}{2}, k + \frac{1}{2})]
\end{aligned}$$

$$\begin{aligned}
H_y^{n+(1/2)}(i + \frac{1}{2}, j, k) &= H_y^{n-(1/2)}(i + \frac{1}{2}, j, k) \\
&\quad - \gamma [E_x^n(i, j, k) - E_x^n(i + 1, j, k) \\
&\quad + E_x^n(i + \frac{1}{2}, j, k + \frac{1}{2}) - E_x^n(i + \frac{1}{2}, j, k - \frac{1}{2})] \\
H_x^{n+(1/2)}(i, j + \frac{1}{2}, k) &= H_x^{n-(1/2)}(i, j + \frac{1}{2}, k) - \gamma [E_y^n(i, j + \frac{1}{2}, k - \frac{1}{2}) \\
&\quad - E_y^n(i, j + \frac{1}{2}, k + \frac{1}{2}) \\
&\quad + E_z^n(i, j + 1, k) - E_z^n(i, j, k)]
\end{aligned}$$



Where $\alpha = (2\varepsilon - \sigma \Delta t) / (2\varepsilon + \sigma \Delta t)$, $\beta = (\Delta t / \Delta x) \cdot [2 / (2\varepsilon + \sigma \Delta t)]$, and

$\gamma = (\Delta t / u \Delta x)$. The superscript of the field variables stands for the time step

(time = $n \cdot \Delta t$), the subscript represents the direction of the field, and (i, j, k)

signifies the node position at $(i\Delta x, j\Delta y, k\Delta z)$.

2.2 A Perfectly Matched Layer for the absorption of Electromagnetic Waves

2.2.1 The theory and derivation of the PML medium

(a) Definition of the PML medium

We will set the equation of a PML medium for two-dimensional problems, first in the TE (transverse electric) case. In Cartesian coordinates let us consider a problem that is without variation along z , with the electric field lying in the (x, y) plane (Fig. 2.3). The electromagnetic field involves three components only, E_x, E_y, H_z , and the Maxwell equations reduce to a set of three equations. In the most general case, which is a medium with an electric conductivity σ and a magnetic conductivity

σ^* , these equations can be written as


$$\begin{aligned} \varepsilon_0 \frac{\partial E_x}{\partial t} + \sigma E_x &= \frac{\partial H_z}{\partial y} \\ \varepsilon_0 \frac{\partial E_y}{\partial t} + \sigma E_y &= -\frac{\partial H_z}{\partial x} \\ u_0 \frac{\partial H_z}{\partial t} + \sigma^* H_z &= \frac{\partial E_x}{\partial y} - \frac{\partial E_y}{\partial x} \end{aligned} \quad (1)$$

Moreover, if the condition

$$\frac{\sigma}{\varepsilon_0} = \frac{\sigma^*}{u_0} \quad (2)$$

is satisfied, then the impedance of the medium (1) equals that of vacuum and no reflection occurs when a plane wave propagates normally across a vacuum-medium interface.

We will now define the PML medium in the TE case. The cornerstone of this definition is the break of the magnetic component H_z into two subcomponents which we will denote as H_{zx} and H_{zy} . In the TE case, a PML medium is defined as a medium in which the electromagnetic field has four components, E_x, E_y, H_{zx}, H_{zy} , connected through the four following equations:

$$\begin{aligned}
 \epsilon_0 \frac{\partial E_x}{\partial t} + \sigma_y E_x &= \frac{\partial(H_{zx} + H_{zy})}{\partial y} \\
 \epsilon_0 \frac{\partial E_y}{\partial t} + \sigma_x E_y &= -\frac{\partial(H_{zx} + H_{zy})}{\partial x} \\
 u_0 \frac{\partial H_{zx}}{\partial t} + \sigma_x^* H_{zx} &= -\frac{\partial E_y}{\partial x} \\
 u_0 \frac{\partial H_{zy}}{\partial t} + \sigma_y^* H_{zy} &= \frac{\partial E_x}{\partial y}
 \end{aligned} \tag{3}$$


where the parameters $(\sigma_x, \sigma_x^*, \sigma_y, \sigma_y^*)$ are homogeneous to electric and magnetic conductivities.

(b) Propagation of a plane wave in a PML medium

Let us consider a wave whose electric field of magnitude E_0 forms an angle φ with the y axis (Fig2.3). We will denote as H_{zx0} and H_{zy0} the magnitudes of the magnetic components H_{zx} and H_{zy} . If a plane wave propagates in the PML medium, then the four components of the field can be expressed as

$$E_x = -E_0 \sin \varphi e^{i\omega(t-\alpha x-\beta y)}$$

$$E_y = E_0 \cos \varphi e^{i\omega(t-\alpha x-\beta y)}$$

$$H_{zx} = H_{zx0} e^{i\omega(t-\alpha x-\beta y)}$$

$$H_{zy} = H_{zy0} e^{i\omega(t-\alpha x-\beta y)} \quad (4)$$

Where ω is the pulsation of the wave, t is the time, and α and β are complex constants. Since the magnitude E_0 is given, the set of Eq.(4) involves four unknown quantities to be determined, $\alpha, \beta, H_{zx0}, H_{zy0}$. Enforcing E_x, E_y, H_{zx}, H_{zy} from (4) in the PML equations (3) yields the following set of equations connecting the four unknowns:

$$\varepsilon_0 E_0 \sin \varphi - i \frac{\sigma_y}{\omega} E_0 \sin \varphi = \beta (H_{zx0} + H_{zy0}) \quad (5)$$

$$\varepsilon_0 E_0 \cos \varphi - i \frac{\sigma_x}{\omega} E_0 \cos \varphi = \alpha (H_{zx0} + H_{zy0}) \quad (6)$$

$$u_0 H_{zx0} - i \frac{\sigma_x^*}{\omega} H_{zx0} = \alpha E_0 \cos \varphi \quad (7)$$

$$u_0 H_{zy0} - i \frac{\sigma_y^*}{\omega} H_{zy0} = \beta E_0 \sin \varphi \quad (8)$$

Obtaining H_{zx0} and H_{zy0} from (7) and (8) and bringing them respectively into (5) and (6) yields

$$\varepsilon_0 u_0 (1 - i \frac{\sigma_y}{\varepsilon_0 \omega}) \sin \varphi = \beta \left[\frac{\alpha \cos \varphi}{(1 - i(\sigma_x^* / u_0 \omega))} + \frac{\beta \sin \varphi}{1 - i(\sigma_y^* / u_0 \omega)} \right] \quad (9)$$

$$\varepsilon_0 u_0 \left(1 - i \frac{\sigma_x}{\varepsilon_0 w}\right) \cos \varphi = \alpha \left[\frac{\alpha \cos \varphi}{(1 - i(\sigma_x^*/u_0 w))} + \frac{\beta \sin \varphi}{1 - i(\sigma_y^*/u_0 w)} \right] \quad (10)$$

This system of two equations connects the unknowns α and β . It may be solved by means of writing the ratio (9) over (10),

$$\frac{\beta}{\alpha} = \frac{\sin \varphi}{\cos \varphi} \frac{1 - i(\sigma_y/\varepsilon_0 w)}{1 - i(\sigma_x/\varepsilon_0 w)} \quad (11)$$

And then obtaining α^2 from (11) and (10) and β^2 from (11) and (9). That yields two sets of (α, β) of opposite signs for two opposite directions of propagation.

Choosing the positive sign we have

$$\alpha = \frac{\sqrt{\varepsilon_0 u_0}}{G} \left(1 - i \frac{\sigma_x}{\varepsilon_0 w}\right) \cos \varphi$$

$$\beta = \frac{\sqrt{\varepsilon_0 u_0}}{G} \left(1 - i \frac{\sigma_y}{\varepsilon_0 w}\right) \sin \varphi \quad (12)$$


$$\text{Where } G = \sqrt{w_x \cos^2 \varphi + w_y \sin^2 \varphi} \quad (13)$$

$$w_x = \frac{1 - i(\sigma_x/\varepsilon_0 w)}{1 - i(\sigma_x^*/u_0 w)} \quad (14)$$

$$w_y = \frac{1 - i(\sigma_y/\varepsilon_0 w)}{1 - i(\sigma_y^*/u_0 w)} \quad (15)$$

Denoting as ψ any component of the field, ψ_0 its magnitude, and c the speed of light, with (4) and (12), we can write

$$\psi = \psi_0 e^{i\omega(t - (x \cos \varphi + y \sin \varphi)/cG)} e^{-(\sigma_x \cos \varphi / \varepsilon_0 cG)x} e^{-(\sigma_y \sin \varphi / \varepsilon_0 cG)y} \quad (16)$$

The last two unknowns H_{zx0} and H_{zy0} can be found as functions of α and β from (7) and (8), and then enforcing the α and β values (12) yields

$$H_{zx0} = E_0 \sqrt{(\varepsilon_0 / u_0)} \frac{1}{G} w_x \cos^2 \varphi$$

$$H_{zy0} = E_0 \sqrt{(\varepsilon_0 / u_0)} \frac{1}{G} w_y \sin^2 \varphi \quad (17)$$

Taking into account (13), the summation of H_{zx0} and H_{zy0} is then

$$H_0 = E_0 \sqrt{(\varepsilon_0 / u_0)} G \quad (18)$$

and the ratio Z of the electric magnitude over the magnetic one is

$$Z = \sqrt{u_0 / \varepsilon_0} \frac{1}{G} \quad (19)$$

For formulas (16) and (19), an important occurrence is when both (σ_x, σ_x^*) and (σ_y, σ_y^*) satisfy the condition(2). Then, the quantities w_x, w_y, G , equal unity at any frequency, and so the expression of the wave components (16) and of the impedance (19) become respectively

$$\psi = \psi_0 e^{iw(t - (x \cos \varphi - y \sin \varphi) / c)} \times e^{-(\sigma_x \cos \varphi / \varepsilon_0 c)x} e^{-(\sigma_y \sin \varphi / \varepsilon_0 c)y} \quad (20)$$

$$Z = \sqrt{u_0 / \varepsilon_0}. \quad (21)$$

(c) Transmission of a Wave through PML-PML Interfaces

In this section, we will address the problem of a plane wave moving from a PML medium to another one. We will prove that in particular cases, with adequate sets of parameters $\sigma_x, \sigma_x^*, \sigma_y, \sigma_y^*$, the transmission is perfect and reflectionless at any incidence angle. These particular cases will be the basis of the perfectly matched

layer.

We first consider the case of two PML media separated by an interface normal to the x axis (fig2-4). Let us denote θ_1 and θ_2 the angles of the incident and transmitted electric fields E_i and E_t , with respect to the interface plane. In the case of (fig.2) we assume the interface to be infinite and incident wave to be plane. First, both the reflected and transmitted waves must be plane too. Second, the ratios of these waves over the incident one must be without variation when moving on the interface. So, for any component ψ of the incident and transmitted fields, and for two points A and B of the interface, we can write

$$\frac{\psi_t(B)}{\psi_i(B)} = \frac{\psi_t(A)}{\psi_i(A)} \quad (22)$$

Denoting as d the distance from A to B, and G_1 , G_2 as the quantities (13) of each media, with (16) we have

$$\psi_t(B) = \psi_i(A) e^{-i\omega(d \sin \theta_1 / cG_1) - (\sigma_{y1} \sin \theta_1 / \varepsilon_0 cG_1)d} \quad (23)$$

$$\psi_t(B) = \psi_i(A) e^{-i\omega(d \sin \theta_2 / cG_2) - (\sigma_{y2} \sin \theta_2 / \varepsilon_0 cG_2)d} \quad (24)$$

Since (22) is true for any distance d , the exponential factors of (23) and (24) must be equal. So the relation

$$(1 - i \frac{\sigma_{y1}}{\varepsilon_0 \omega}) \frac{\sin \theta_1}{G_1} = (1 - i \frac{\sigma_{y2}}{\varepsilon_0 \omega}) \frac{\sin \theta_2}{G_2} \quad (25)$$

Must be satisfied, where

$$G_k = \sqrt{w_{xk} \cos^2 \theta_k + w_{yk} \sin^2 \theta_k} \quad (\text{for } k=1,2). \quad (26)$$

Let us now consider the incident, reflected, and transmitted electric and magnetic fields $E_i, E_r, E_t, H_i, H_r, H_t$ (fig.2.4). First, continuity of the fields E_y and

$H_{zx} + H_{zy}$ lying in the interface yields the following set of equations:

$$E_i \cos \theta_1 - E_r \cos \theta_1 = E_t \cos \theta_2 \quad (27)$$

$$H_i + H_r = H_t \quad (28)$$

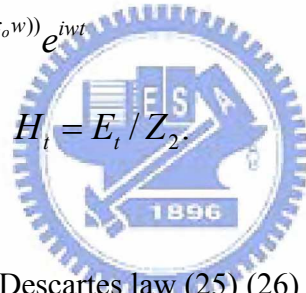
Second, denoting as E_{io}, E_{ro}, E_{to} , the magnitudes of E_i, E_r, E_t , and setting $x=0$ in the interface, with (2.2.11) and (2.2.14) we can write

$$E_i = E_{io} e^{-iw(y \sin \theta_1 / cG_1)(1-i(\sigma_{y1} / \epsilon_0 w))} e^{iwt} \quad (29)$$

$$E_r = E_{ro} e^{-iw(y \sin \theta_1 / cG_1)(1-i(\sigma_{y1} / \epsilon_0 w))} e^{iwt} \quad (30)$$

$$E_t = E_{to} e^{-iw(y \sin \theta_2 / cG_2)(1-i(\sigma_{y2} / \epsilon_0 w))} e^{iwt} \quad (31)$$

$$H_i = E_i / Z_1, \quad H_r = E_r / Z_1, \quad H_t = E_t / Z_2 \quad (32)$$



As a consequence of the Snell-Descartes law (25),(26),the three exponentials on space of (29),(30),(31) are equal. So, reporting E_i, \dots, H_t from (29),(30),(31) into (27),(28) this system (27),(28)becomes

$$E_{io} \cos \theta_1 - E_{ro} \cos \theta_1 = E_{to} \cos \theta_2 \quad (33)$$

$$\frac{E_{io}}{Z_1} + \frac{E_{ro}}{Z_1} = \frac{E_{to}}{Z_2} \quad (34)$$

Defining the reflection factor as the ratio of the electric components in the interface, that is, $-E_{ro} \cos \theta_1 / E_{io} \cos \theta_1$, and then solving the set (33),(34) for this ratio, the reflection factor r_p for the TE case is

$$r_p = \frac{Z_2 \cos \theta_2 - Z_1 \cos \theta_1}{Z_2 \cos \theta_2 + Z_1 \cos \theta_1} \quad (35)$$

With (19), we can rewrite (35) as

$$r_p = \frac{G_1 \cos \theta_2 - G_2 \cos \theta_1}{G_1 \cos \theta_2 + G_2 \cos \theta_1} \quad (36)$$

where G_1 and G_2 are functions of θ_1 and θ_2 through (26)

Let us consider an interface lying between media having same σ_y and σ_y^*

conductivities, that is, a $(\sigma_{x1}, \sigma_{x1}^*, \sigma_y, \sigma_y^*)$ and $(\sigma_{x2}, \sigma_{x2}^*, \sigma_y, \sigma_y^*)$ media. Then

the (25) becomes

$$\frac{\sin \theta_1}{G_1} = \frac{\sin \theta_2}{G_2} \quad (37)$$

If, moreover, the two media are matched ones, that is, $(\sigma_{x1}, \sigma_{x1}^*)$, $(\sigma_{x2}, \sigma_{x2}^*)$, and

(σ_y, σ_y^*) satisfying (2), we have $G_1 = G_2 = 1$, so (37) reduces to

$$\theta_1 = \theta_2 \quad (38)$$

And the reflection factor (36) is then

$$r_p = 0 \quad (39)$$

The general frame of the PML technique is pointed out on Fig.2.5.

As a summary of this section we can now say that the reflection factor

between two PML media whose conductivities satisfy (2) is null:

These are

🚩 the reflection factor is null at an interface normal to x lying between a vacuum

and a $(\sigma_x, \sigma_x^*, 0, 0)$ matched medium or between a $(0, 0, \sigma_y, \sigma_y^*)$ and a

$(\sigma_x, \sigma_x^*, \sigma_y, \sigma_y^*)$ matched media.

the reflection factor is null at an interface normal to y lying between a vacuum and a $(0, 0, \sigma_y, \sigma_y^*)$ matched medium or between a $(\sigma_x, \sigma_x^*, 0, 0)$ and a $(\sigma_x, \sigma_x^*, \sigma_y, \sigma_y^*)$ matched media.

Let us consider, for instance, the upper-right part of a gridded computational domain (Fig2-6). With the usual FDTD notations, (3.b) and (3.c) yield the following equations that can be applied in the whole layer, except in the interface for E_y (see below),

$$E_y^{n+1}(i, j + 1/2) = e^{-\sigma_x(i)\Delta t / \epsilon_0} E_y^n(i, j + 1/2) - \frac{(1 - e^{-\sigma_x(i)\Delta t / \epsilon_0})}{\sigma_x(i)\Delta x} \times [H_{zx}^{n+1/2}(i + 1/2, j + 1/2) + H_{zy}^{n+1/2}(i + 1/2, j + 1/2) - H_{zx}^{n+1/2}(i - 1/2, j + 1/2) - H_{zy}^{n+1/2}(i - 1/2, j + 1/2)] \quad (40)$$

$$H_{zx}^{n+1}(i + 1/2, j + 1/2) = e^{-\sigma_x^*(i+1/2)\Delta t / u_0} H_{zx}^{n+1/2}(i + 1/2, j + 1/2) - \frac{(1 - e^{-\sigma_x^*(i+1/2)\Delta t / u_0})}{\sigma_x^*(i + 1/2)\Delta x} \times [E_y^n(i + 1, j + 1/2) - E_y^n(i, j + 1/2)], \quad (41)$$

Where σ_x and σ_x^* are functions of x(I).(on Fig2-6) For the E_y component lying in the interface, the magnetic field has one component H_z on one side and two subcomponents H_{zx}, H_{zy} on the other. That is a result of using the Maxwell equations in the inner volume, but it has no physical significance. The finite difference equations have to be modified. So, in the right side interface normal to x, (40) becomes

$$\begin{aligned}
E_y^{n+1}(il, j+1/2) &= e^{-\sigma_x(il)\Delta t/\varepsilon_0} E_y^n(il, j+1/2) \\
&\frac{(1 - e^{-\sigma_x(il)\Delta t/\varepsilon_0})}{\sigma_x^*(il)\Delta x} \\
&\times [H_{zx}^{n+1/2}(il+1/2, j+1/2) + E_{zy}^{n+1/2}(il+1/2, j+1/2) - H_z^{n+1/2}(il-1/2, j+1/2)].
\end{aligned} \tag{42}$$

2.3 Numerical Stability Condition

In the two-dimension case

$$\Delta t \leq \frac{1}{c \sqrt{\frac{1}{\Delta x^2} + \frac{1}{\Delta y^2}}} = \frac{\Delta}{c_o \sqrt{2}}$$

and $\Delta x = \Delta y = \Delta$

2.4 Numerical Dispersion Relation

In the two-dimension TE(TM) case

$$\left[\frac{1}{c\Delta t} \sin\left(\frac{w\Delta t}{2}\right) \right]^2 = \left[\frac{1}{\Delta x} \sin\left(\frac{\tilde{k}_x \Delta x}{2}\right) \right]^2 + \left[\frac{1}{\Delta y} \sin\left(\frac{\tilde{k}_y \Delta y}{2}\right) \right]^2$$

where \tilde{k}_x and \tilde{k}_y are, respectively, the x- and y-components of the numerical wavevector, and w is the wave angular frequency. To quantitatively assess the dependence of numerical dispersion upon FD-TD grid discretization, we shall take as the case, assuming for simplicity square unit cells ($\Delta x = \Delta y = \Delta$) and wave propagation at an angle α with respect to the positive x-axis ($\tilde{k}_x = \tilde{k} \cos \alpha$; $\tilde{k}_y = \tilde{k} \sin \alpha$). Then numerical dispersion relation () simplifies to

$$\left(\frac{\Delta}{c\Delta t}\right)^2 \sin^2\left(\frac{w\Delta t}{2}\right) = \sin^2\left(\frac{\Delta \cdot \tilde{k} \cos \alpha}{2}\right) + \sin^2\left(\frac{\Delta \cdot \tilde{k} \sin \alpha}{2}\right)$$

By applying the following Newton's method iterative procedure:

$$\widetilde{k}_{i+1} = \widetilde{k}_i - \frac{\sin^2(A\widetilde{k}_i) + \sin^2(B\widetilde{k}_i) - C}{A\sin(2A\widetilde{k}_i) + B\sin(2B\widetilde{k}_i)}$$

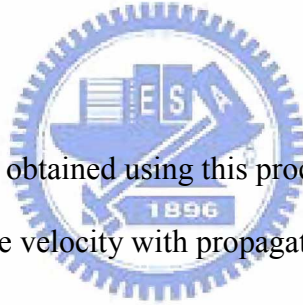
$$A = \frac{\Delta \cdot \cos \alpha}{2}, \quad B = \frac{\Delta \cdot \sin \alpha}{2}, \quad C = \left(\frac{\Delta}{c\Delta t}\right)^2 \sin^2\left(\frac{w\Delta t}{2}\right)$$

So we can obtain the numerical wavevector \widetilde{k}_{final} that the numerical phase velocity

\widetilde{v}_p is given by

$$\widetilde{v}_p = \frac{w}{\widetilde{k}_{final}}$$

See figure.2-7 graphs results obtained using this procedure that illustrate the variation of the numerical phase velocity with propagation angle in a two-dimensional FDTD grid.



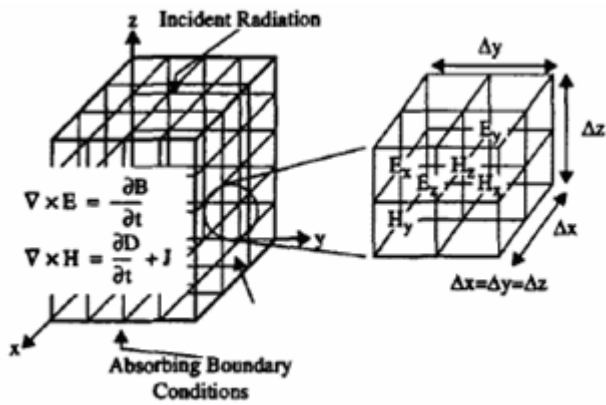


Fig2.1 Maxwell's equations are solved over a cubic grid using the FDTD method. The field components are staggered over the grid.

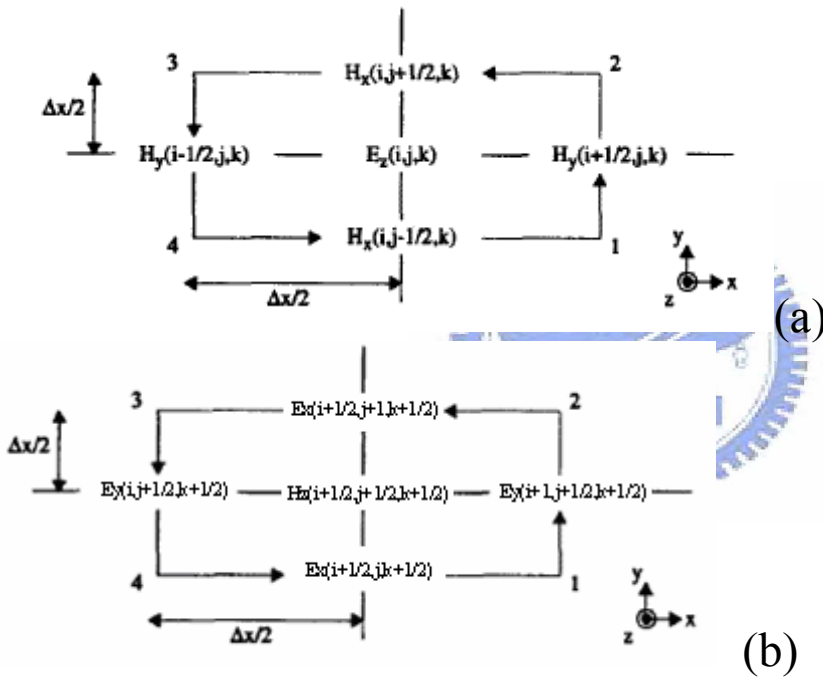


Fig2.2-(a) The electric field $E_z(i,j,k)$ is calculated by summing up the magnetic field values of the four neighboring nodes. The magnetic field components are assumed to be constant along the line segments 1-2, 2-3, 3-4, and 4-1, and the electric field E_z is assumed to be constant over the square surface bounded by 1-2-3-4.

(b) The magnetic field $H_z(i+1/2,j+1/2,k+1/2)$ is calculated by summing up the electric field values of the four neighboring nodes. The electric field components are assumed to be constant along the line segments 1-2, 2-3, 3-4, and 4-1, and the magnetic field H_z is assumed to be constant over the square surface bounded by 1-2-3-4.

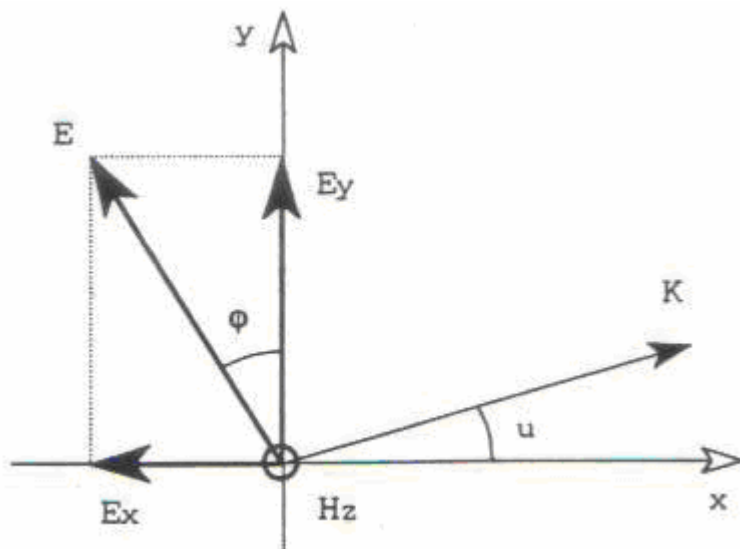


Fig-2.3 The transverse electric problem

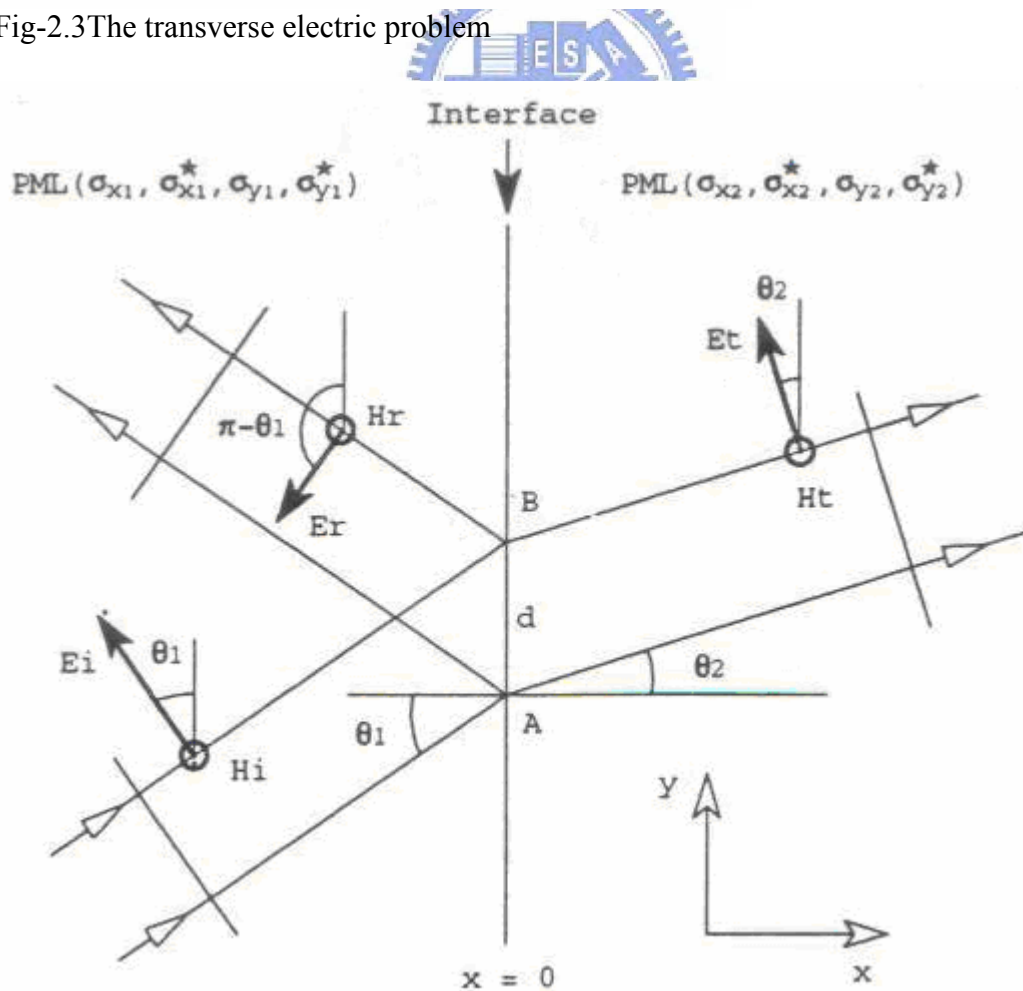


Fig-2.4 Interface lying between two PML media.

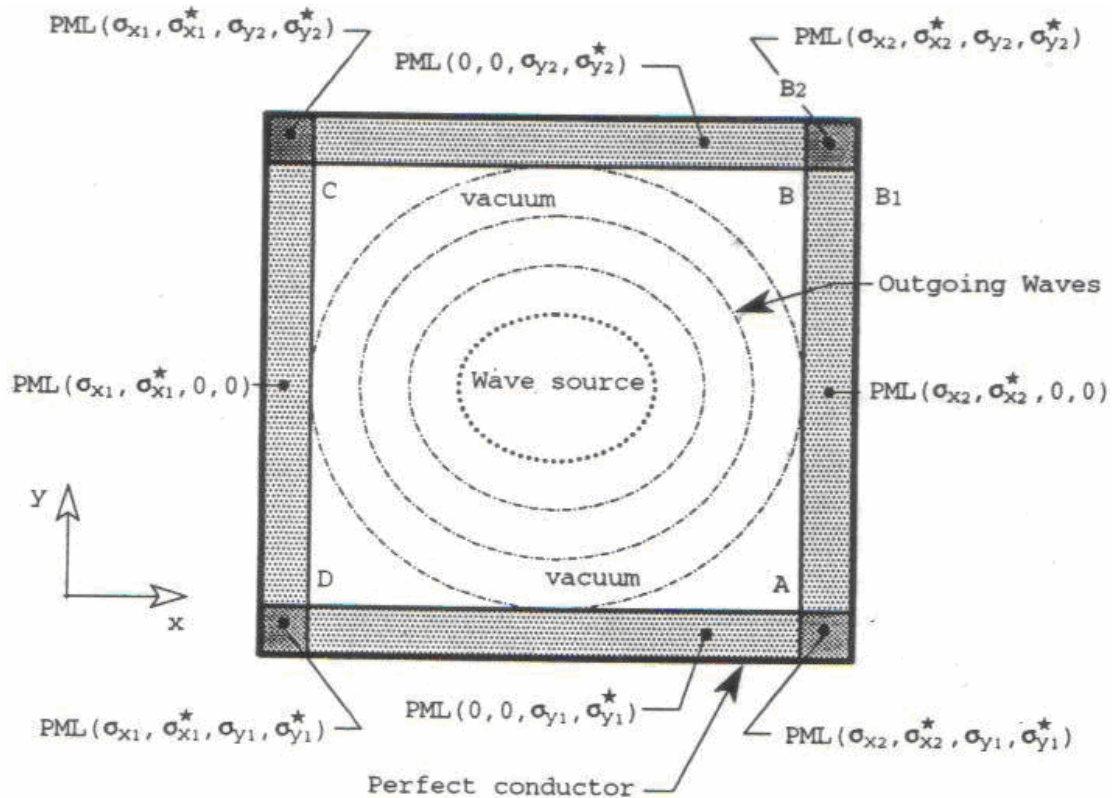


Fig-2.5 The PML technique.

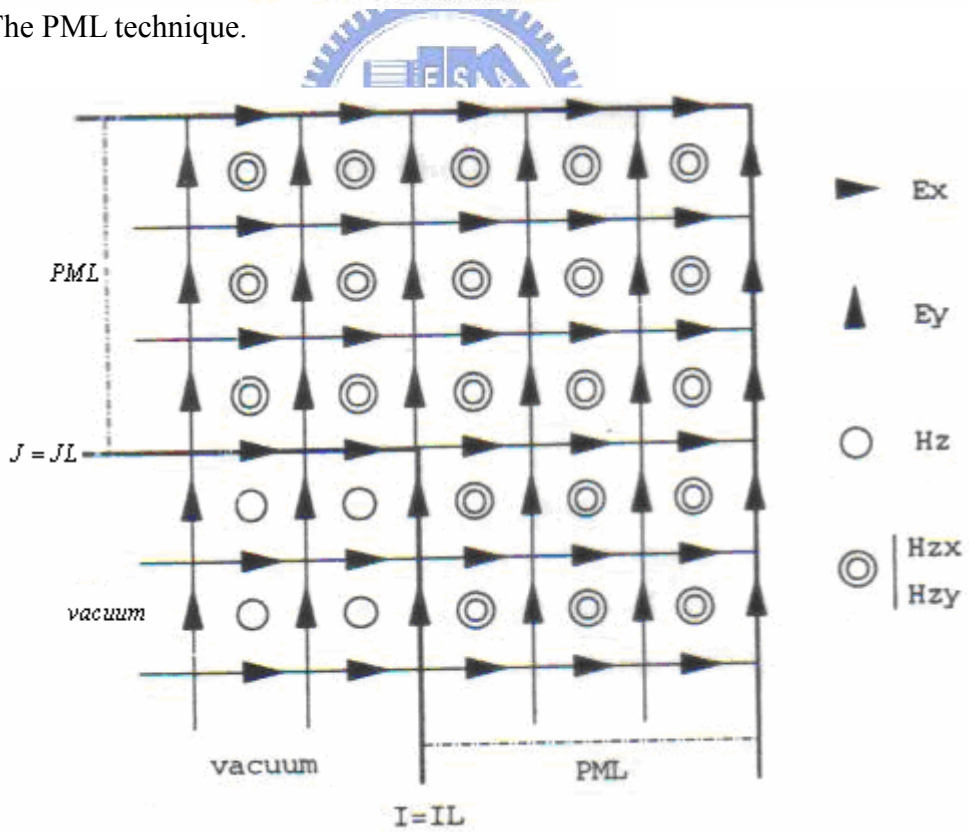


Fig-2.6 Upper-right part of the FDTD grid

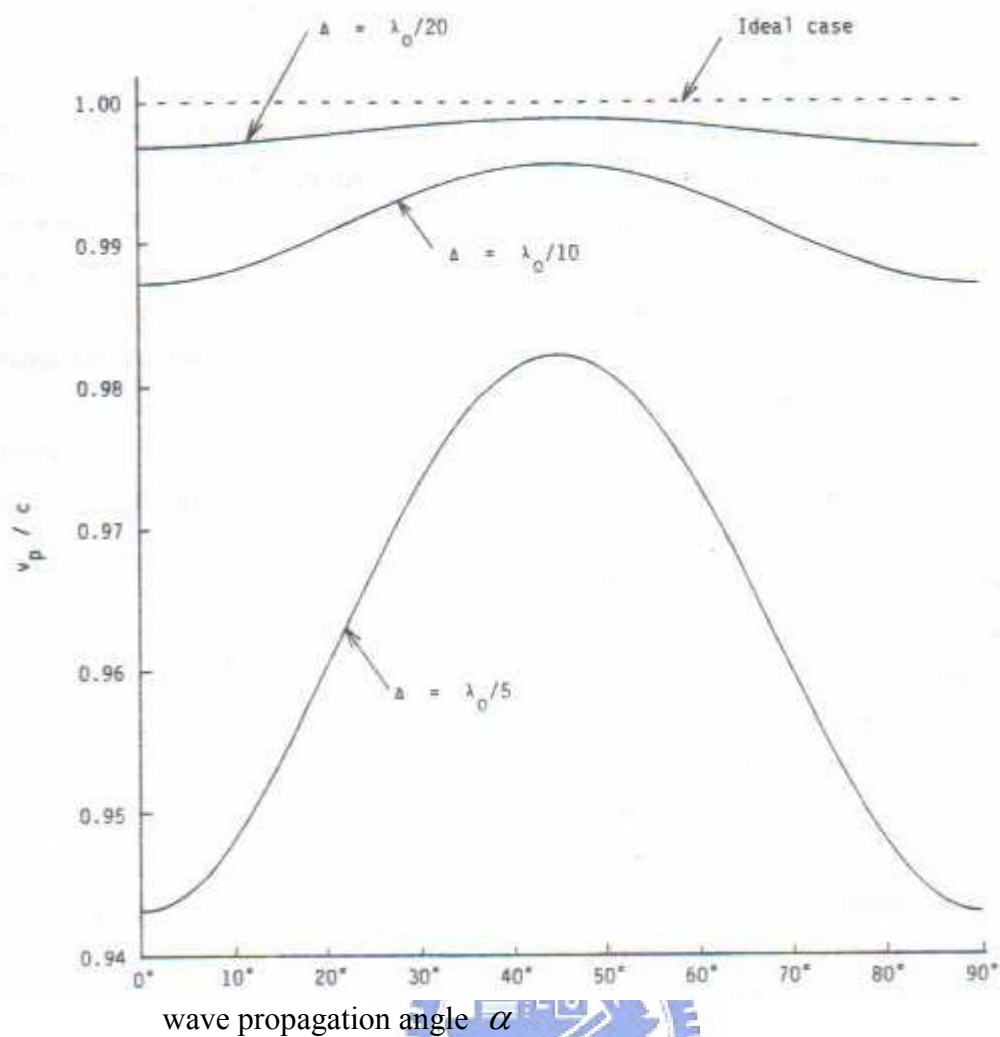


Figure.2-7 graphs results obtained using this procedure that illustrate the variation of the numerical phase velocity with propagation angle in a two-dimensional FDTD grid.

Chapter 3

Using Battle-Lemarie Scaling Function Based Multiresolution time-domain(MRTD) schemes

3.1 Fundamentals Of Multiresolution Analysis

In literature [1], [2], the use of scaling and wavelet functions as a complete set of basis functions is called multiresolution analysis. The most important properties of the scaling and wavelets functions defining a multiresolution analysis are now summarized:

1. All scaling and wavelet functions are localized both in the frequency and the space/time domains.
2. The Fourier transform of a scaling function(Fig.3-1) is a low-pass function(Fig.3-2), while the Fourier transform of the corresponding mother wavelet(Fig.3-3) is a bandpass function(Fig.3-4). This implies that, in a multiresolution expansion, scaling functions can be utilized to sample the low-frequency content of the field/signal, while wavelets sample the high-frequency content.
3. The scaling function of one resolution level, m , are orthonormal to the scaling functions of the same resolution level, but not the scaling functions of other resolution levels:

$$\langle \phi_{mn}, \phi_{mv} \rangle = \delta_{nv} \quad (3-1)$$

This implies that, when using scaling functions in an expansion, we cannot mix different resolution levels.

4. The scaling function are orthogonal to all wavelets of any higher-order resolution level:

$$\langle \phi_{mn}, \psi_{uv} \rangle = 0 \quad m \leq u \quad (3-2)$$

while the wavelet function of any resolution level are orthonormal to all other wavelets at any resolution level:

$$\langle \psi_{mn}, \psi_{uv} \rangle = \delta_{mu} \delta_{nv} \quad (3-3)$$

The above two properties allow us to mix scaling functions of one resolution level with wavelets of one or more resolution levels of the same or higher order, m.

5. Any scaling function of m resolution can be expanded in the form of wavelets of all lower resolution levels:

$$\phi_{mn}(x) = \sum_{j=-\infty}^{m-1} \sum_{i=-\infty}^{\infty} d_{ji}^{mn} \psi_{ji}(x) \quad (3-4)$$

3-2 Derivation of the S-MRTD Scheme

The S-MRTD and W-MRTD schemes[12] are derived using cubic spline Battle-Lemarie scaling and wavelet functions .

At first, for simplicity, we will only derive the S-MRTD scheme for a homogeneous medium. The derivation is similar to that of Yee's FDTD scheme which uses the method of moments[19] with pulse functions as expansion and test functions. For the derivation of S-MRTD, the field components are represented by a series of scaling functions in space and pulse functions in time.

2-D (TE) S-MRTD Scheme:

Maxwell's vector equation

$$\nabla \times H = \varepsilon \frac{\partial E}{\partial t} \quad (1)$$

$$\nabla \times E = -u_0 \frac{\partial H}{\partial t} \quad (2)$$

for a homogeneous medium with the permittivity ε and the permeability u_0 may

be written in the form of three scalar Cartesian equations as

$$\frac{\partial H_z}{\partial y} = \varepsilon \frac{\partial E_x}{\partial t} \quad (3)$$

$$-\frac{\partial H_z}{\partial x} = \varepsilon \frac{\partial E_y}{\partial t} \quad (4)$$

$$\frac{\partial E_x}{\partial y} - \frac{\partial E_y}{\partial x} = u_0 \frac{\partial H_z}{\partial t} \quad (5)$$



The electric and magnetic field components incorporated in these equations are expanded as following

$$E_x(\vec{r}, t) = \sum_{k,l,m=-\infty}^{+\infty} {}_k E_{l+1/2,m}^{\phi x} h_k(t) \phi_{l+1/2}(x) \phi_m(y)$$

$$E_y(\vec{r}, t) = \sum_{k,l,m=-\infty}^{+\infty} {}_k E_{l,m+1/2}^{\phi y} h_k(t) \phi_l(x) \phi_{m+1/2}(y)$$

$$H_z(\vec{r}, t) = \sum_{k,l,m=-\infty}^{+\infty} {}_{k+1/2} H_{l+1/2,m+1/2}^{\phi z} h_{k+1/2}(t) \phi_{l+1/2}(x) \phi_{m+1/2}(y) \quad (6)$$

where ${}_k E_{l,m}^{\phi K}$ and ${}_k H_{l,m}^{\phi K}$ with $K= x, y$ are the coefficients for the field

expansions in terms of scaling functions. The indexes $l, m,$ and k are the discrete

space and time indices related to the space and time coordinates via $x = l\Delta x$, $y = m\Delta y$ and $y = k\Delta t$, where $\Delta x, \Delta y$ and Δt represent the space and time discretization intervals in x -, y - and t -direction. The function $h_m(x)$ is defined as

$$h_m(x) = h\left(\frac{x}{\Delta x} - m\right) \quad (7)$$

with the rectangular pulse function

$$h(x) = \begin{cases} 1 & \text{for } |x| < 1/2 \\ 1/2 & \text{for } |x| = 1/2 \\ 0 & \text{for } |x| > 1/2 \end{cases} \quad (8)$$

The function $\phi_m(x)$ is defined as

$$\phi_m(x) = \phi\left(\frac{x}{\Delta x} - m\right) \quad (9)$$

where $\phi(x)$ represents the spline Battle-Lemarie scaling function [13], [14] depicted in Fig. 3-1. Assuming the Fourier transformation

$$\tilde{\phi}(\lambda) = \int_{-\infty}^{+\infty} \phi(x) e^{j\lambda x} dx \quad (10)$$

and

$$\phi(x) = \frac{1}{2\pi} \int_{-\infty}^{+\infty} \tilde{\phi}(\lambda) e^{-j\lambda x} d\lambda \quad (11)$$

Respectively, the closed-form expression of the scaling function in spectral domain is given by

$$\tilde{\phi}(\lambda) = \left(\frac{\sin(\frac{\lambda}{2})}{\frac{\lambda}{2}} \right)^4 \cdot \frac{1}{\sqrt{1 - \frac{4}{3} \sin^2(\frac{\lambda}{2}) + \frac{2}{5} \sin^4(\frac{\lambda}{2}) - \frac{4}{315} \sin^6(\frac{\lambda}{2})}} \quad (12)$$

with the low-pass spectral domain characteristics shown in Fig.3-2.

We insert the field expansions in Maxwell's equations and sample the equations using pulse functions as test functions in time and scaling functions as test functions in space. For the sampling with respect to time, we need the following integrals[10]

$$\int_{-\infty}^{+\infty} h_m(x)h_{m'}(x)dx = \delta_{m,m'}\Delta x \quad (13)$$

where $\delta_{m,m'}$ represents the kronecker symbol

$$\delta_{m,m'} = \begin{cases} 1 & \text{for } m = m' \\ 0 & \text{for } m \neq m' \end{cases} \quad (14)$$

and

$$\int_{-\infty}^{+\infty} h_m(x) \frac{\partial h_{m'+1/2}(x)}{\partial x} dx = \delta_{m,m'} - \delta_{m,m'+1} \quad (15)$$

For the sampling with respect to space, we use the orthogonality relation for the scaling functions [17]

$$\int_{-\infty}^{+\infty} \phi_m(x)\phi_{m'}(x)dx = \delta_{m,m'}\Delta x. \quad (16)$$

To calculate the integral corresponding to (15) for scaling functions, we make use of the closed form expression of the scaling function in spectral domain. According to Galerkin's method [7], for complex basis functions, one has to choose the complex conjugant of the basis functions as test functions. We then obtain

$$\int_{-\infty}^{+\infty} \phi_m(x) \frac{\partial \phi_{m'+1/2}(x)}{\partial x} dx = \frac{1}{\pi} \int_0^{\infty} |\tilde{\phi}(\lambda)|^2 \lambda \sin \lambda(m' - m + 1/2) d\lambda \quad (17)$$

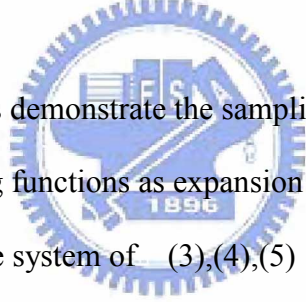
where $\tilde{\phi}(\lambda)$ is given by (12). This integral may be evaluated numerically resulting in

$$\int_{-\infty}^{+\infty} \phi_m(x) \frac{\partial \phi_{m'+1/2}(x)}{\partial x} dx = \sum_{i=-\infty}^{+\infty} a(i) \delta_{m+i,m'} \quad (18)$$

The coefficients $a(i)$ for $0 \leq i \leq 8$ are shown in Table I, and the coefficients $a(i)$ for $i < 0$ are given by the symmetry relation $a(-1-i)=-a(i)$. The Battle-Lemarie scaling function does not have compact but only exponential decaying support and thus, the coefficients $a(i)$ for $i > 8$ are not zero. However, we found that these coefficients are negligible, affecting the accuracy of the field computation only for very low values of the wave vector. We therefore use the approximation

$$\int_{-\infty}^{+\infty} \phi_m(x) \frac{\partial \phi_{m'+1/2}(x)}{\partial x} dx \approx \sum_{i=-9}^{+8} a(i) \delta_{m+i,m'} \quad (19)$$

in order to obtain a MRTD scheme useful for practical applications.



For sake of simplicity, let us demonstrate the sampling of Maxwell's equations by using only scaling functions as expansion and testing functions. By applying Galerkin's method, the system of (3),(4),(5) takes the form:

$$\begin{aligned} {}_{k+1} E_{l+1/2,m}^{\phi x} &= {}_k E_{l+1/2,m}^{\phi x} + \frac{\Delta t}{\varepsilon \Delta y} \left[\sum_{i=-9}^{+8} a(i) {}_{k+1/2} H_{l+1/2,m+i+1/2}^{\phi z} \right] \\ {}_{k+1} E_{l,m+1/2}^{\phi y} &= {}_k E_{l,m+1/2}^{\phi y} + \frac{\Delta t}{\varepsilon \Delta x} \left[- \sum_{i=-9}^{+8} a(i) {}_{k+1/2} H_{l+i+1/2,m+1/2}^{\phi z} \right] \\ {}_{k+1/2} H_{l+1/2,m+1/2}^{\phi z} &= {}_{k-1/2} H_{l+1/2,m+1/2}^{\phi z} + \frac{\Delta t}{u_0 \Delta} \left[\sum_{i=-9}^{+8} a(i) {}_k E_{l+1/2,m+i}^{\phi x} - \sum_{i=-9}^{+8} a(i) {}_k E_{l+i,m+1/2}^{\phi y} \right] \end{aligned} \quad (20)$$

where l, m , and k are the discrete space and time indices. In fact, the total field at a particular space point for the S-MRTD scheme may be calculated from the field expansions, see (6), by sampling them with delta test functions in space and time

domain. For example, the x-component of the total electric field

$E_x(\vec{r}_o, t_o) = E_x(x_o, y_o, t_o)$ at an arbitrary space point \vec{r}_o at time t_o with $(k - 1/2)\Delta t < t_o < (k + 1/2)\Delta t$ is given by

$$E_x(\vec{r}_o, t_o) = \iiint E_x(\vec{r}, t) \delta(x - x_o) \delta(y - y_o) \delta(t - t_o) dx dy dt$$

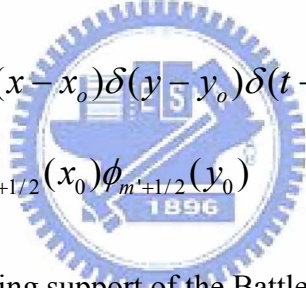
$$= \sum_{l', m', n'=-\infty}^{+\infty} E_{l'+1/2, m'}^{\phi x} \phi_{l'+1/2}(x_o) \phi_{m'}(y_o)$$

$$E_y(\vec{r}_o, t_o) = \iiint E_y(\vec{r}, t) \delta(x - x_o) \delta(y - y_o) \delta(t - t_o) dx dy dt$$

$$= \sum_{l', m', n'=-\infty}^{+\infty} E_{l', m'+1/2}^{\phi y} \phi_{l'}(x_o) \phi_{m'+1/2}(y_o)$$

$$H_z(\vec{r}_o, t_o) = \iiint H_z(\vec{r}, t) \delta(x - x_o) \delta(y - y_o) \delta(t - t_o) dx dy dt$$

$$= \sum_{l', m', n'=-\infty}^{+\infty} H_{l'+1/2, m'+1/2}^{\phi z} \phi_{l'+1/2}(x_o) \phi_{m'+1/2}(y_o)$$



Due to the exponentially decaying support of the Battle-Lemarie scaling function (see Figure.3-1), only a few terms of this two-dimensional summation have to be considered.

3-3 Numerical Stability condition

In the two-dimension case and $\Delta x = \Delta y = \Delta$

$$\Delta t_{S-MRTD} \leq \frac{1}{c_o \left(\sum_{i=0}^{15} |a(i)| \right) \sqrt{\frac{1}{\Delta x^2} + \frac{1}{\Delta y^2}}} = 0.6371 \cdot \frac{\Delta}{c_o \sqrt{2}}$$

3-4 Numerical Dispersion

To calculate the numerical dispersion[14] of the S-MRTD scheme, plane monochromatic traveling-wave trial solutions are substituted in the discretized Maxwell's equations. For example, the E_x, E_y, H_z components for the TE mode has the form

$$\begin{aligned}
 {}_k E_{l,m}^{\phi x} &= E_{x0} \exp\left(j(\tilde{k}_x l \Delta x + \tilde{k}_y m \Delta x - wk \Delta t)\right) \\
 {}_k E_{l,m}^{\phi y} &= E_{y0} \exp\left(j(\tilde{k}_x l \Delta x + \tilde{k}_y m \Delta x - wk \Delta t)\right) \\
 {}_k H_{l,m}^{\phi z} &= H_{z0} \exp\left(j(\tilde{k}_x l \Delta x + \tilde{k}_y m \Delta x - wk \Delta t)\right)
 \end{aligned} \tag{21}$$

Where \tilde{k}_x and \tilde{k}_y are the x- and y-components of the numerical wave vector and w is the wave angular frequency. Substituting the above expressions into (20), the following numerical dispersion relation is obtained for the TE mode of the S-MRTD scheme after algebraic manipulation:

$$\begin{aligned}
 \left(\frac{\Delta}{c \Delta t} \cdot \sin\left(\frac{w \Delta t}{2}\right)\right)^2 &= \left[\sum_{i'=0}^{n_a-1} a(i') \sin\left(\tilde{k} \cos \phi (i'+1/2)\Delta\right)\right]^2 + \\
 &\left[\sum_{j'=0}^{n_a-1} a(j') \sin\left(\tilde{k} \sin \phi (j'+1/2)\Delta\right)\right]^2
 \end{aligned} \tag{22}$$

Where $\Delta x = \Delta y = \Delta$ and wave propagating at ϕ with respect to x-axis ($\tilde{k}_x = \tilde{k} \cos \phi$ and $\tilde{k}_y = \tilde{k} \sin \phi$). Defining the Courant number $C = \frac{c \Delta t}{\Delta}$ and the number of cells per wavelength $R = \lambda_{real} / \Delta$ and using the definition of the

wave vector $\tilde{k} = (2\pi) / \lambda_{NUM}$, the dispersion relationship can be written as

$$\left(\frac{1}{C} \cdot \sin\left(\frac{\pi C}{R}\right) \right)^2 = \left[\sum_{i'=0}^{n_a-1} a(i') \sin\left(\left(\frac{2\pi}{R}\right) \left(\frac{\lambda_{real}}{\lambda_{NUM}}\right) \cos \phi(i'+1/2) \right) \right]^2 + \left[\sum_{j'=0}^{n_a-1} a(j') \sin\left(\left(\frac{2\pi}{R}\right) \left(\frac{\lambda_{real}}{\lambda_{NUM}}\right) \sin \phi(j'+1/2) \right) \right]^2 \quad (23)$$

Upon numerical solution of (23) by applying the bisection-Newton-Raphson hybrid

technique for different values n_a, θ , and C, we obtain $\tilde{k} = (2\pi) / \lambda_{NUM}$.

Substituting $\tilde{k} = (2\pi) / \lambda_{NUM}$ into $V_{NUM} = \frac{w}{\tilde{k}}$, we can obtain the phase error

introduced by the MRTD

algorithm. **(Figure.3-5)**



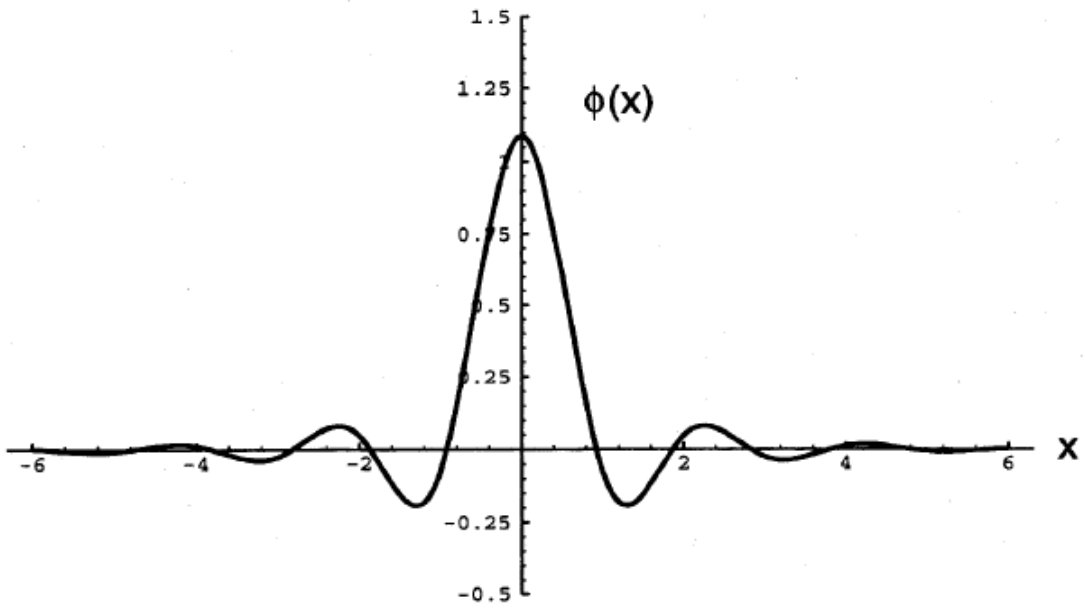


Figure.3-1 Cubic spline Battle-Lemarie scaling function in space domain.

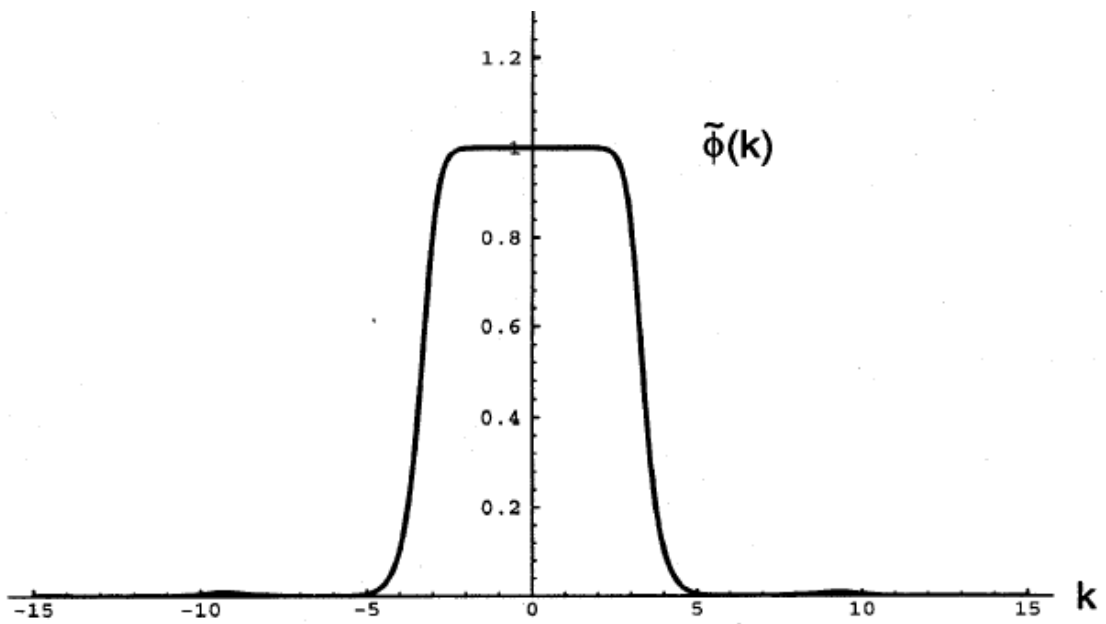
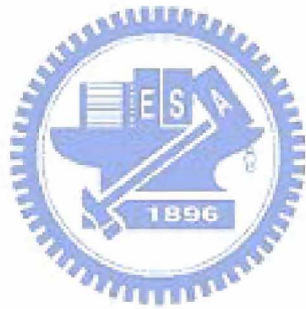


Figure.3-2 Cubic spline Battle-Lemarie scaling function in spectral domain.

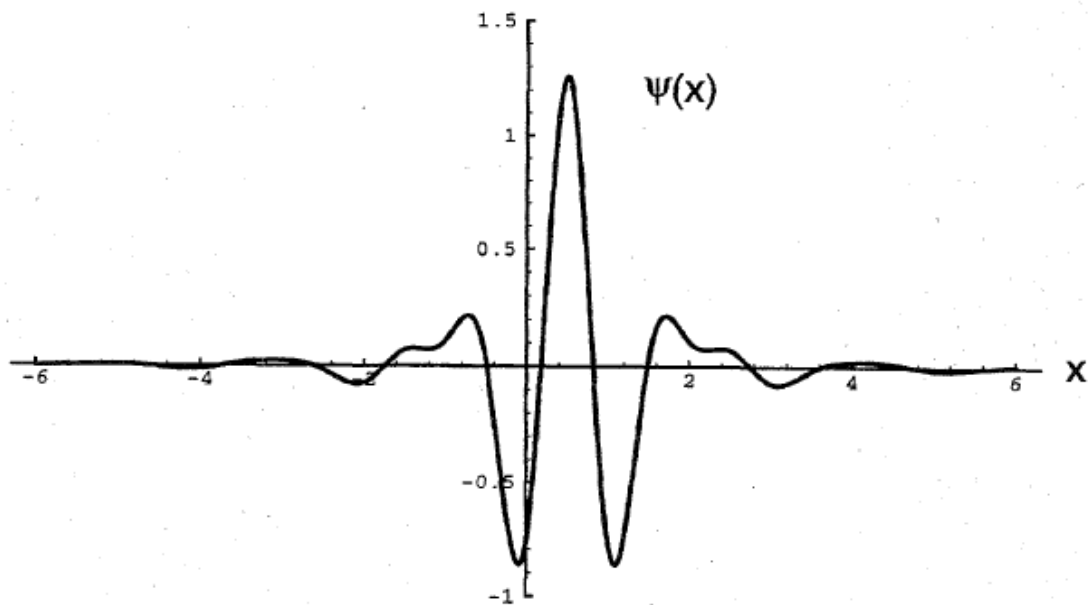


Figure.3-3 Cubic spline Battle-Lemarie wavelet function in space domain.

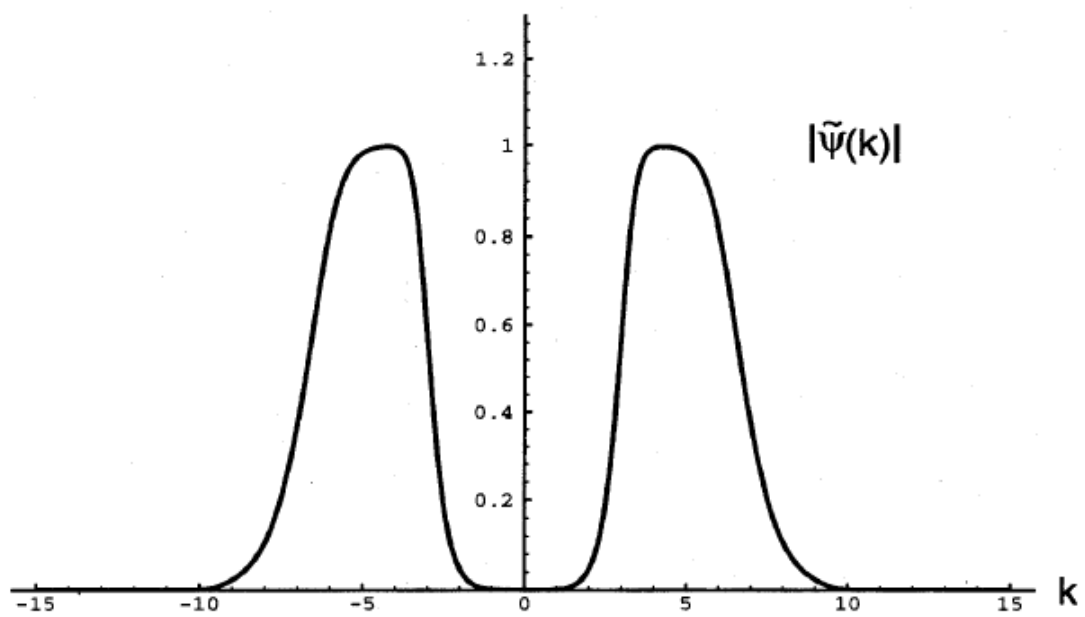


Figure.3-4 Cubic spline Battle-Lemarie wavelet function in spectral domain.

i	$a(i)$
0	1.29161604157839
1	-0.155978843323672
2	5.9606303324687290E-02
3	-2.929157759806890E-02
4	1.5362399457426780E-02
5	-8.184462325283712E-03
6	4.3757585552354830E-03
7	-2.342365356649461E-03
8	1.252877717042020E-03
9	-6.716635068590737E-04
10	3.583506907489797E-04
11	-1.931321684715780E-04
12	1.019327767057869E-04
13	-5.613943183518454E-05
14	2.834596805928539E-05
15	-1.700348604873522E-05



Table I Coefficients $a(i)$

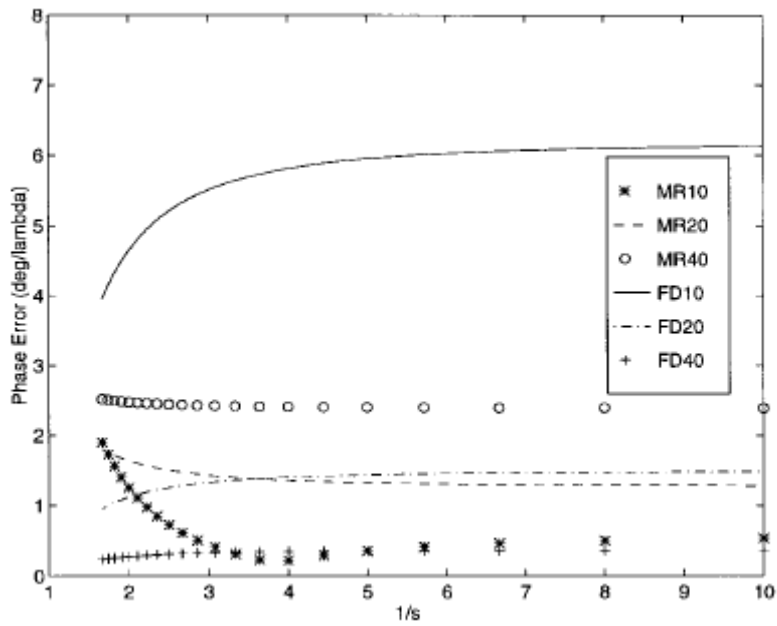
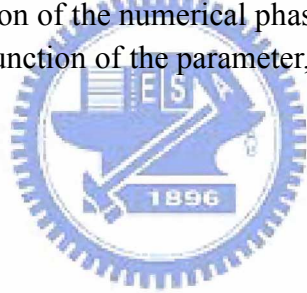


Figure.3-5 Phase error of MRTD employing scaling functions only:
 Graphs the variation of the numerical phase error in degrees per wavelength as a function of the parameter, $1/s(1/C)$, for the case $n_a = 8$.



Chapter 4

Discussion and Conclusion

4.1 S-MRTD formulation

In the PML medium, we can obtain the equations(4.0) from chapter 2.

$$\begin{aligned}
 \varepsilon_0 \frac{\partial E_x}{\partial t} + \sigma_y E_x &= \frac{\partial(H_{zx} + H_{zy})}{\partial y} \\
 \varepsilon_0 \frac{\partial E_y}{\partial t} + \sigma_x E_y &= -\frac{\partial(H_{zx} + H_{zy})}{\partial x} \\
 u_0 \frac{\partial H_{zx}}{\partial t} + \sigma_x * H_{zx} &= -\frac{\partial E_y}{\partial x} \\
 u_0 \frac{\partial H_{zy}}{\partial t} + \sigma_y * H_{zy} &= \frac{\partial E_x}{\partial y}
 \end{aligned} \tag{4.0}$$

Upon applying Galerkin's technique, the following is obtained by S-MRTD method

$$\begin{aligned}
 {}_{k+1}E_{l+1/2,m}^{\phi x} &= e^{-\frac{\sigma_y(m)\Delta t}{\varepsilon_0}} \cdot {}_k E_{l+1/2,m}^{\phi x} + \frac{1 - e^{-\frac{\sigma_y(m)\Delta t}{\varepsilon_0}}}{\sigma_y(m)\Delta y} \cdot \\
 &\left[\sum_{i=-9}^{+8} a(i) \cdot ({}_{k+1/2}H_{l+1/2,m+1/2+i}^{\phi zx} + {}_{k+1/2}H_{l+1/2,m+1/2+i}^{\phi zy}) \right]
 \end{aligned} \tag{4.1}$$

$${}_{k+1}E_{l,m+1/2}^{\phi y} = e^{\frac{-\sigma_x(l)\Delta t}{\varepsilon_0}} \cdot {}_kE_{l,m+1/2}^{\phi y} - \frac{1 - e^{\frac{-\sigma_x(l)\Delta t}{\varepsilon_0}}}{\sigma_x(l)\Delta x} \quad (4.2)$$

$$\left[\sum_{i=-9}^{+8} a(i) \cdot ({}_{k+1/2}H_{l+1/2+i,m+1/2}^{\phi zx} + {}_{k+1/2}H_{l+1/2+i,m+1/2}^{\phi zy}) \right]$$

$${}_{k+1/2}H_{l+1/2,m+1/2}^{\phi zx} = e^{\frac{-\sigma_x^*(l+1/2)\Delta t}{\mu_0}} \cdot {}_{k-1/2}H_{l+1/2,m+1/2}^{\phi zx} - \frac{1 - e^{\frac{-\sigma_x^*(l+1/2)\Delta t}{\varepsilon_0}}}{\sigma_x^*(l+1/2)\Delta x} \cdot \left[\sum_{i=-9}^{+8} a(i) {}_kE_{l+i,m+1/2}^{\phi y} \right] \quad (4.3)$$

$${}_{k+1/2}H_{l+1/2,m+1/2}^{\phi zy} = e^{\frac{-\sigma_y^*(m+1/2)\Delta t}{\mu_0}} \cdot {}_{k-1/2}H_{l+1/2,m+1/2}^{\phi zy} + \frac{1 - e^{\frac{-\sigma_y^*(m+1/2)\Delta t}{\varepsilon_0}}}{\sigma_y^*(m+1/2)\Delta y} \cdot \left[\sum_{i=-9}^{+8} a(i) {}_kE_{l+1/2,m+i}^{\phi x} \right] \quad (4.4)$$

In main grid (figure 4-1), we use the equations (4.5) from chapter 3.

$${}_{k+1}E_{l+1/2,m}^{\phi x} = {}_kE_{l+1/2,m}^{\phi x} + \frac{\Delta t}{\varepsilon \Delta y} \left[\sum_{i=-9}^{+8} a(i) {}_{k+1/2}H_{l+1/2,m+i+1/2}^{\phi z} \right]$$

$${}_{k+1}E_{l,m+1/2}^{\phi y} = {}_kE_{l,m+1/2}^{\phi y} + \frac{\Delta t}{\varepsilon \Delta x} \left[- \sum_{i=-9}^{+8} a(i) {}_{k+1/2}H_{l+i+1/2,m+1/2}^{\phi z} \right] \quad (4.5)$$

$${}_{k+1/2}H_{l+1/2,m+1/2}^{\phi z} = {}_{k-1/2}H_{l+1/2,m+1/2}^{\phi z} + \frac{\Delta t}{u_0 \Delta} \left[\sum_{i=-9}^{+8} a(i) {}_kE_{l+1/2,m+i}^{\phi x} - \sum_{i=-9}^{+8} a(i) {}_kE_{l+i,m+1/2}^{\phi y} \right]$$

4.2 Simulation results

In this thesis, we simulate a new contact hole 2D-PSM design (figure 4-7) [15], which will be compatible with dense contact-hole. When it is applied together with QUASAR OAI, we can enhance the printing resolution to achieve an excellent DOF (figure 4-8). When we proceed to simulate this 3D-mask (figure 4-9), we can find the DOF degraded to 50 percent. (figure 4-10)

When we use our program by S-MRTD, we can make the actual reflection waves are short successfully. (see figure 4-2,3,4,5,6)

Accordingly, we can continue to simulate 2D-mask by the program.



4.3 Conclusion

The multiresolution time-domain method has been successfully applied to rigorous 2D mask diffraction simulation with PML. MRTD requires only about 3.5 to 3.9 nodes per wavelength to achieve a phase error of two degrees per wavelength or less, while FDTD requires 19 nodes per wavelength or more to achieve the same phase error (Table 1). As a result, MRTD is faster than the speed of FDTD for the same level of accuracy. Figure 4- show the dispersion characteristics of FDTD and S-MRTD

Then, the development of the MRTD-PML absorber enhances the applicability of the MRTD technique to complex 2(3)-D open geometries while maintaining the high computational efficiency in terms of memory and execution time requirements.

After having completed the work related above, one way of further research were initiated: the implementation of the three-dimensional S-MRTD simulation in order to achieve a more detailed analysis for the wave-structure(MASK) interaction problem.

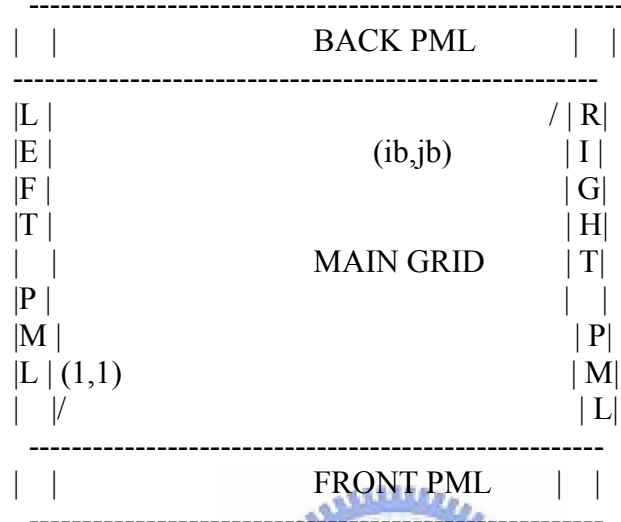


Figure 4-1 The PML regions are labeled as shown in the diagram

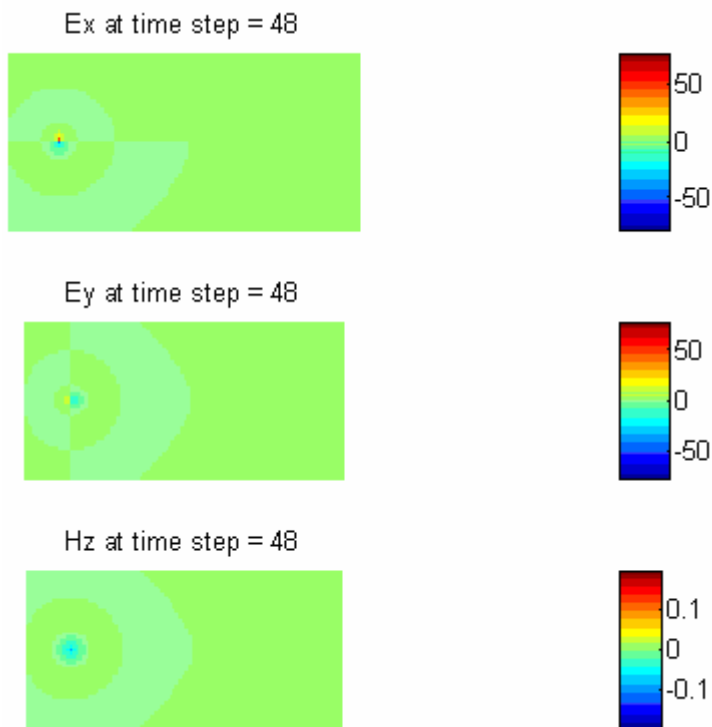
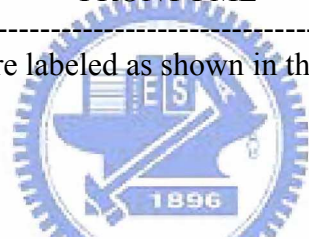


Figure4-2 MRTD simulation result

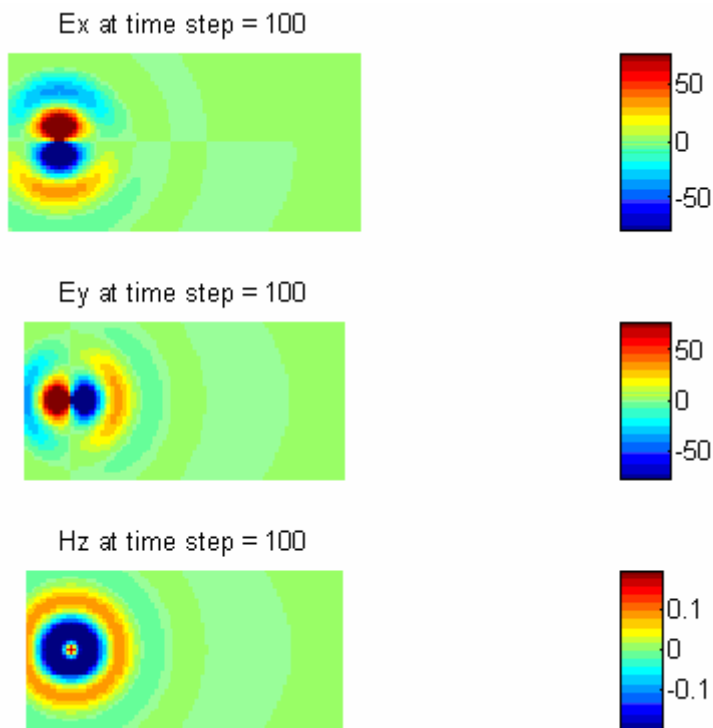


Figure 4-3 MRTD simulation result

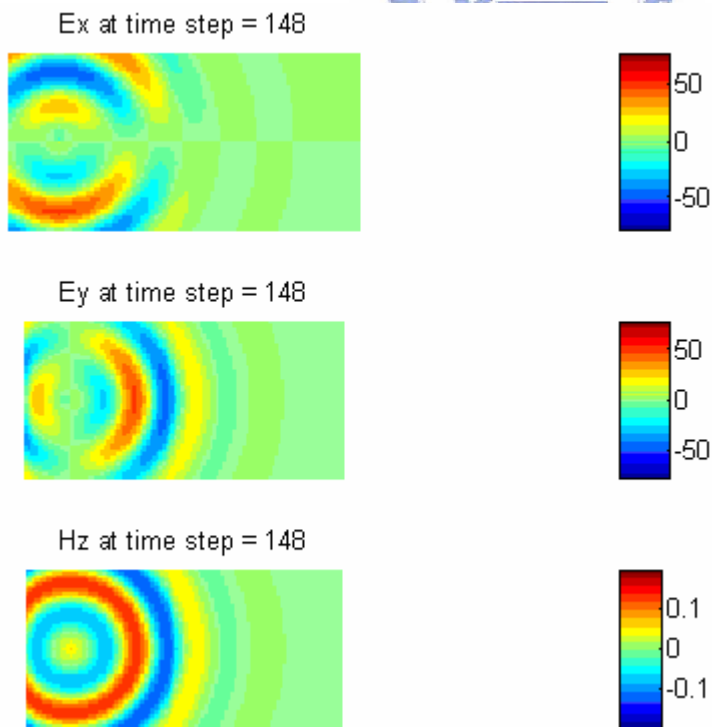


Figure 4-4 MRTD simulation result

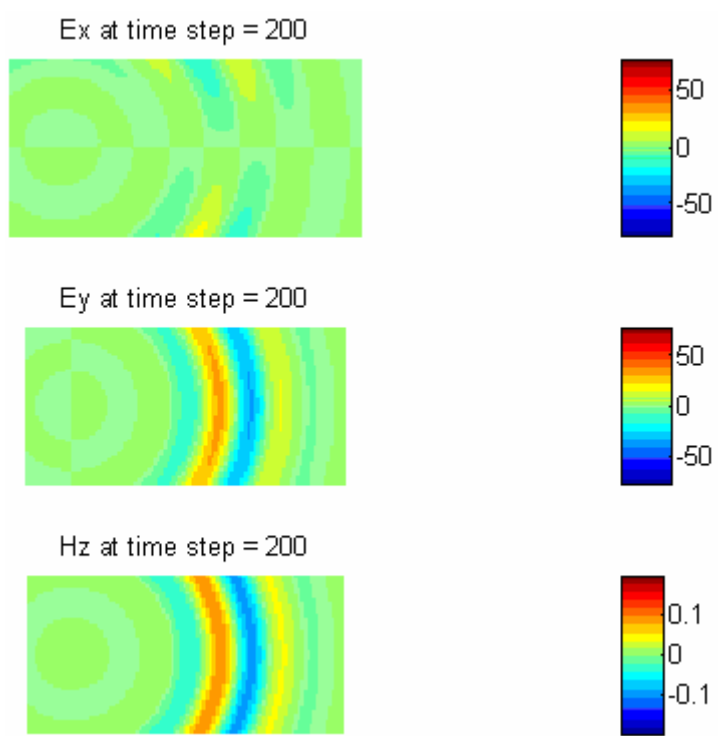


Figure 4-5 MRTD simulation result

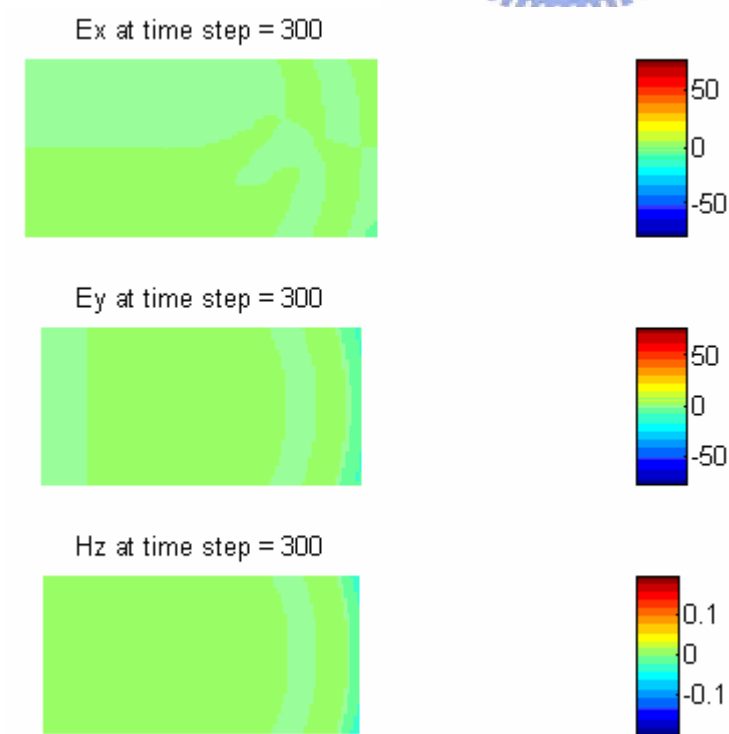
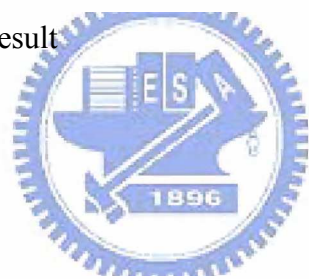


Figure 4-6 MRTD simulation result

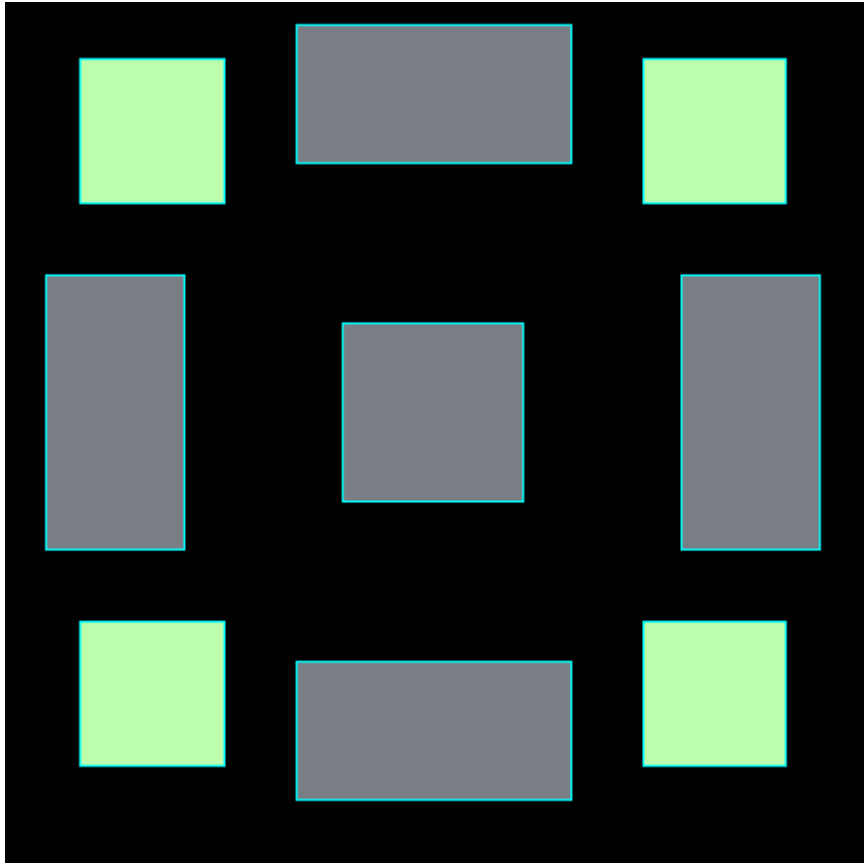
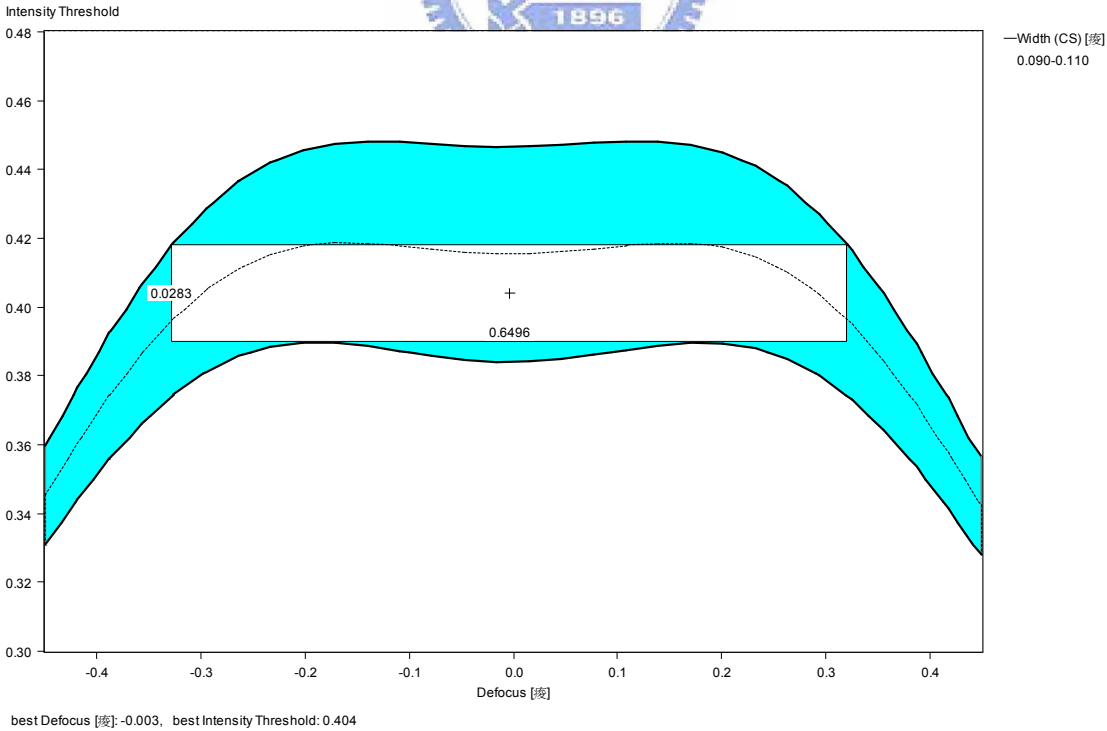
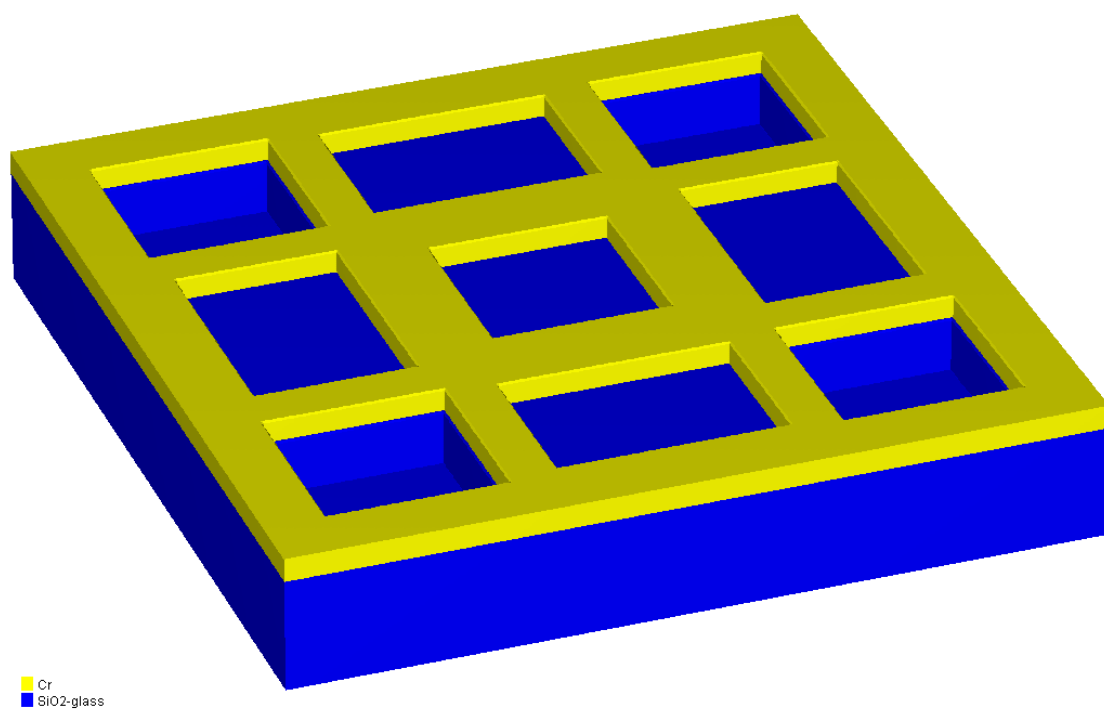


Figure 4-7 A new contact hole 2D-PSM design



DOF=0.6496 um

Figure 4-8 E-D curve of 100nm contact-hole by the 2D-PSM design



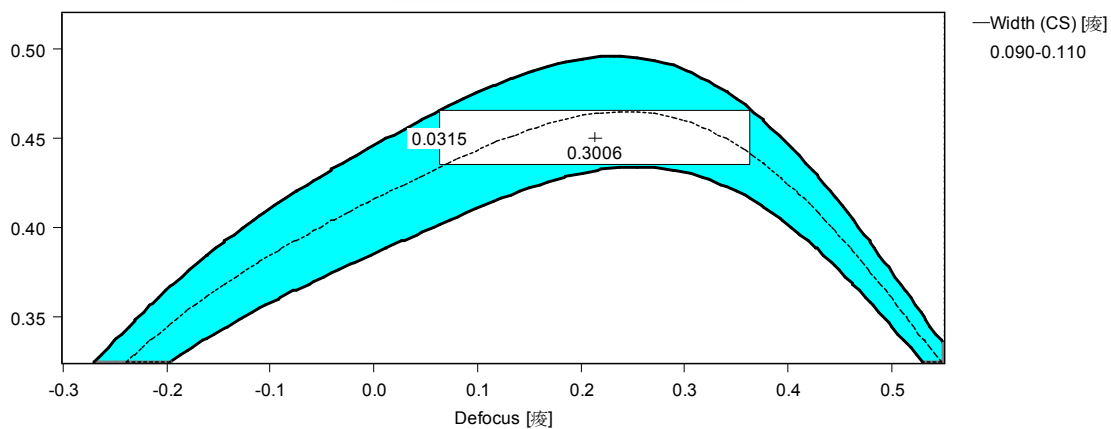
Cr
SiO2-glass

SOLID-C®

Figure 4-9 A new contact hole 3D-PSM design



Intensity Threshold



best Defocus [micrometers]: 0.215, best Intensity Threshold: 0.450

SOLID-C®

DOF=0.3006um

Figure 4-10 E-D curve of 100nm contact-hole by the 3D-PSM design

Table 1: FDTD (left) versus MRTD (right) for 2D Quartz Object

Nodes/ λ in air (quartz)	Phase error per λ	Nodes/ λ in air (quartz)	Phase error per λ
96.5 (64.3)	0°	7.7 (5.1)	1.4°
19.3 (12.9)	4.3°	3.9 (2.6)	2.0°
15.4 (10.3)	6.9°	3.5 (2.3)	3.2°
12.5 (8.3)	11.2°	3.1 (2.1)	3.4°

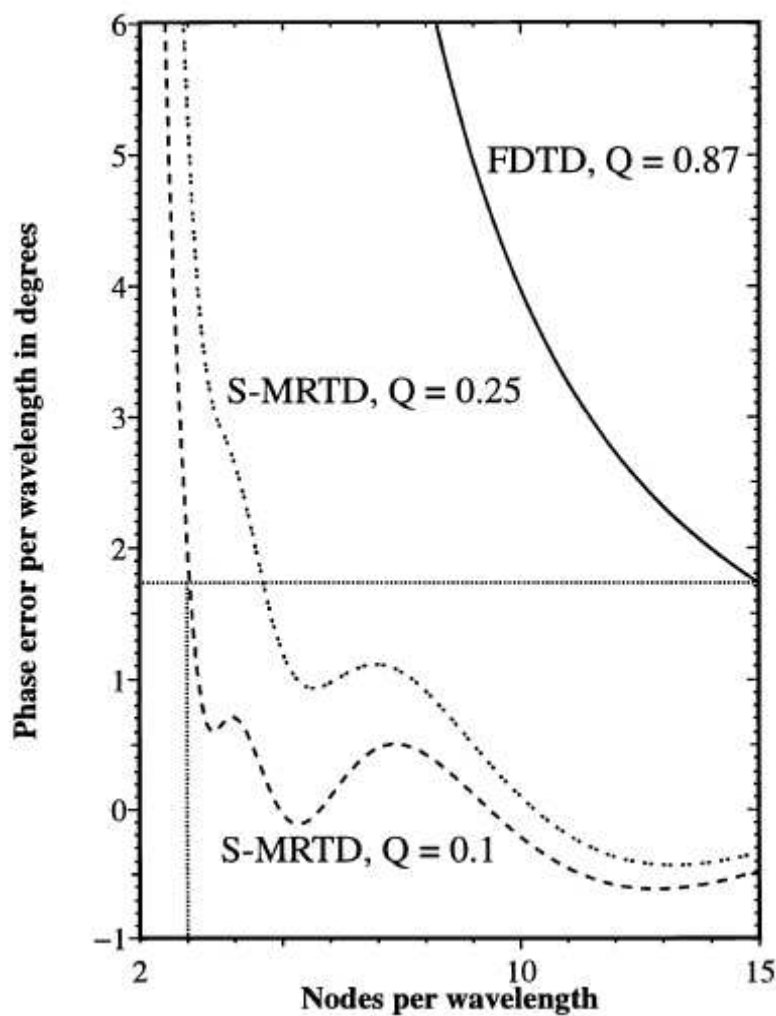
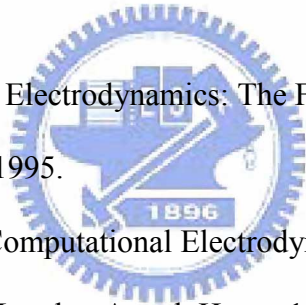


Figure 4-11 Dispersion characteristics of FDTD and S-MRTD, $Q = c\Delta t / \Delta x$

References

- [1] S. G. Mallat, "A theory for multiresolution signal decomposition: The wavelet representation," IEEE Trans. Pattern Anal. Machine Intell., vol. 11, pp. 674-693, July 1989.
- [2] B. Jawerth and W. Sweldens, "An overview of wavelet based multiresolution analyses," SIAM Rev., vol. 36, no. 3, pp. 377-412, Sept. 1994.
- [3] J. D. Plummer, P. B. Griffin, and M. D. Deal, Silicon VLSI technology: fundamentals, practice, and modeling, Pearson Education, first ed., 2000.
- [4] B. J. Lin, Optical lithography, SPIE, first ed., 2002.
- [5] M. Born and E. Wolf, principles of optics, 7th ed. (1999)
- [6] G. Furter, "High-resolution high-apertured objective." U. S. patent #5880891, Apr. 1997.
- [7] J. W. Goodman; "Introduction to Fourier Optics", Third ed (2005).
- [8] D. C. Cole, "Derivation and simulation of Higher Numerical Aperture Scalar Aerial Images", Jpn. J. Appl. Phys. Vol. 31 (1992) pp. 4110-4119
- [9] M. S. Yeung, "Extension of the Hopkins theory of partially coherent imaging to include thin-film interference effects", SPIE Vol. 1927 Optical/Laser Microlithography (1993)
- [10] J. P. Berenger, "A Perfectly Matched Layer for the Absorption of Electromagnetic Waves", J. Comput. Phys. 114, 185 (1994).
- [11] B. J. Lin, "Thin-film optimization strategy in high numerical aperture optical lithography part 1: principles", J. Microelectromechanical Systems, 14(4), 2005
- [12] M. Krumpholtz and L. P. B. Katehi, "MRTD: New Time Domain Schemes Based on Multiresolution Analysis", IEEE Trans. Microwave Theory Tech., vol. 44, pp. 555-561 (1996)

- [13]K. S. Yee,"Numerical solution of Initial Boundary Value Problems Involving Maxwell's Equations in Isotropic Media", IEEE Trans. Antenna. Propag. 14, 302 (1966).
- [14] Emmanouil M. Tentzeris," Stability and Dispersion Analysis of Battle-Lemarie-Based MRTD Schemes", IEEE transactions on microwave , vol. 47, no. 7, 1999
- [15] Chang, Chung-Hsing "Novel contact hole reticle design for enhanced lithography process window in IC manufacturing" , Proc. of SPIE. vol. SPIE-5645, pp.32-43. 2005
- [16] A.K.Wong,"Wave-optical considerations in photolithography",Proceedings Of SPIE vol.5182(2003)
- [17]TAFLOVE,Computational Electrodynamics: The Finite-Difference Time-Domain Method.Boston:Artech House,1995.
- [18] TAFLOVE,Advances in Computational Electrodynamics:The Finite-Difference Time-Domain Method.Boston,London:Artech House,1998
- [19] R. F. Harrington, Field Computation by Moment Methods. Malabar,FL: Krieger , 1982.
- [20] A.K.Wong , A R.Neureuther,"Polarization effects in mask Transmission" , SPIE vol.1674 Optical/Laser Microlithography(1992)



個人簡歷

姓名：曾建彰

性別：男

出生年月日：民國 71 年 11 月 14 日

住址：高雄市苓雅區正大路 120 之 5 號

學歷：

國立高雄大學電機工程系學士 (91.9-94.6)

國立交通大學電子研究所碩士 (94.9-96.7)



碩士論文題目：

二維完美匹配層應用於多重解析法之光學微影模擬

Two-Dimensional Perfectly Matched Layer Applied to Multiresolution Time-Domain Method for Optical lithography simulation